Performance Analysis of a Square Lattice PCF Based Surface Plasmon Resonance Sensor

by

Md Abdullah-Al-Mamun

Student No: 0412062274

MASTER OF SCIENCE IN ELECTRICAL AND ELECTRONIC ENGINEERING

Department of Electrical and Electronic Engineering

BANGLADESH UNIVERSITY OF ENGINEERING AND TECHNOLOGY

December 2014

The thesis titled **"Performance Analysis of a Square Lattice PCF Based Surface Plasmon Resonance Sensor"** submitted by Md Abdullah-Al-Mamun, Student No.: 0412062274 F, Session: April, 2012, has been accepted as satisfactory in partial fulfillment of the requirement for the degree of MASTER OF SCIENCE IN ELECTRICAL AND ELECTRONIC ENGINEERING on December 13, 2014.

BOARD OF EXAMINERS

1. _____

Dr. Md. Shah Alam — Chairman
Professor — (Supervisor)
Department of Electrical and Electronic Engineering,
BangladeshUniversity of Engineering and Technology,
Dhaka-1000, Bangladesh.

2. _____

Dr. Taifur Ahmed Chowdhury — Member
Professor and Head — (Ex-officio)
Department of Electrical and Electronic Engineering,
BangladeshUniversity of Engineering and Technology,
Dhaka-1000, Bangladesh.

3. _____

Dr. Farseem Mannan Mohammedy — Member
Associate Professor
Department of Electrical and Electronic Engineering,
BangladeshUniversity of Engineering and Technology,
Dhaka-1000, Bangladesh.

4. _____

Gp Capt Dr. Md Hossam-E-Haider — Member
Senior Instructor — (External)
Department of Electrical, Electronic and Communication Engineering (EECE),
Military Institute of Science and Technology (MIST),
Mirpur Cantonment, Dhaka-1216, Bangladesh.

CANDIDATE'S DECLARATION

It is hereby declared that this thesis or any part of it has not been submitted elsewhere for the award of any degree or diploma and that all sources are acknowledged.

Signature of the Candidate

_____

Md Abdullah-Al-Mamun

Dedication

To my parents

Acknowledgement

First of all, I would like to thank Allah, the almighty, for giving me the ability to complete this thesis work.

I would like to express my greatest respect and deepest appreciation to my supervisor, Professor Dr. Md. Shah Alam. I have greatly benefited from his enthusiasm, knowledge, guidance and sharp thoughts on broad scientific topics. Moreover, his inspiration, encouragement, patience and wisdom provided me invaluable support during the past two and half years of study in BUET. Dr. Md. Shah Alam is the most important person who taught me the way to do an in-depth study and the right attitude to conduct research. When I went to the wrong direction, he led me back to the right track. He is an extremely talented scientist with thousands of ideas. I would also like to express my sincere appreciation to him for letting me pursue a number of ideas during this study. His support to pursue creative thoughts and critical analysis has contributed most significantly to the development of this thesis. The outcome of this research would never be possible without his constant encouragement, support and the freedom in research that he gave to me. I owe him so much that thank you is not enough to express my deep gratitude.

I would like to express my sincere appreciation to all my teachers from Bangladesh University of Engineering and Technology. The knowledge I gathered from the classes gave me deep understanding about numerous topics and worked as stepping stone towards the formulation of my thesis. The projects and assignments from the classes also helped me to conceptualize and conduct this investigation.

Special thanks must go to Assistant professor Md. Asiful Islam for all his support, direction and friendship. He taught me not only about photonics but also helped me in finite element simulation and Matlab calculation. He also encouraged me all the time and helped me on every little thing, even on checking my paper, guiding on writing etc.

Finally and most significantly, I would like to thank my parents and family members. I am so glad to have their unconditional support during this special period of my life. Without their constant love and everlasting understanding I would not have had the strength to finish this work.

ABSTRACT

In this dissertation, photonic crystal fiber (PCF) based surface plasmon resonance (SPR) sensor has been investigated. Conventionally, hexagonal lattice PCF with modified structure is often used in SPR sensing probe. Being simpler in structural geometry than hexagonal lattice PCF, square lattice PCF is investigated for its suitability in SPR sensing system. Square lattice structure is modified to construct multiple cores with centrally located analyte channel. Designing the sensor with only one analyte channel has reduced the amount of gold required for coating. The amount of analyte required for effective detection and also the co-channel interference from neighboring channel is expected to be reduced. Use of multiple cores has effectively increased the overlap between core guided light and surface plasmons, resulting better sensitivity. Besides, performance parameters like sensitivity, detection accuracy or signal-to-noise ratio (SNR), sensing range and detection linearity has been evaluated. Factors contributing to the refractive index sensitivity like metal coating width, use of different metal for coating, bimetallic layer, different doping concentration etc. are explored systematically through design, simulation, data acquisition, data interpretation and analysis. The proposed design successfully contributed in the excitation of SPPs and confirmed the suitability of square lattice PCF for SPR sensing system. The proposed design with gold coating yielded a sensitivity of 7432 nm/RIU in the sensing range of 1.43 to 1.50 refractive index. It has also resulted in achieving a SNR of 1.202. The detection linearity obtained is also very high (0.99911). The suitability of other metal such as silver and copper has also been studied. Silver and copper did not show better sensitivity than gold but exhibited promise in enhancement of SNR. It is also found that silver and copper cannot be used without protective coating because of oxidation, corrosion and chemical reactivity. As sensitivity also depends on the core material, different doping concentration has also been used to tune the sensitivity. Doping concentration of 13.5% GeO_2, 9.1 % P_2O_5 and 5.2 % B_2O_3 has been used separately with pure silica. Doping with 13.5% GeO_2 yielded better sensitivity than pure silica with a value of 8411 nm/RIU, while other two dopants resulted less sensitivity than pure silica. To utilize the potential of silver to produce better SNR, the sensitivity and SNR of the sensor is further tailored by the use of bimetallic layer consisting gold and silver. Investigation with bimetallic layer yielded a sensitivity of 13180 nm/RIU. The SNR also got enhanced from a value of 1.202 to 1.32. With these findings, this study offered a modified approach for PCF based SPR sensor probe, encompassing a promise of enhanced performance and simplicity in design and fabrication.

CONTENTS

LIST OF TABLES

LIST OF FIGURES

LIST OF ABBREVIATIONS

ATR	:	Attenuated Total internal Reflection
FEA	:	Finite Element Analysis
FEM	:	Finite Element Method
HF	:	Holey Fiber
H-PCF	:	Hexagonal-Lattice Photonic Crystal Fiber
PBG	:	Photonic Band Gap
PCF	:	Photonic Crystal Fiber
PML	:	Perfectly Matched Layer
RIU	:	Refractive Index Unit
SL-PCF	:	Square-Lattice Photonic Crystal Fiber
SNR	:	Signal-to-Noise Ratio
SPP	:	Surface Plasmon Polariton
SPR	:	Surface Plasmon Resonance
TE	:	Transverse Electric
TIR	:	Total Internal Reflection
TM	:	Transverse Magnetic

LIST OF SYMBOLS

n	:	Refractive Index
β	:	Propagation constant
α	:	Attenuation constant
Λ	:	Pitch of a PCF
d	:	Air hole diameter in a PCF
ε	:	Permittivity (or dielectric constant)
ω	:	Angular frequency
k	:	Wave vector
δ	:	Skin depth
τ	:	Average collision time of free electrons
ω_p	:	Plasma frequency

CHAPTER 1

INTRODUCTION

1.1 Surface plasmons

The phenomenon reported by Wood as merely an anomalous decrease in the intensity of light reflected by a metal grating was not labeled by the term surface plasmons in 1902 but gave birth of an exploding research field of present time named as plasmonics [1]. Surface plasmons are actually charge density oscillations along the metal-dielectric interface which constitutes an electromagnetic field coupled to the oscillations of plasma at metal surface. Surface plasmons are excited at particular resonance condition. After the dawning age, step-wise advances in the physics of surface plasmons have been made by several outstanding researchers [2]. It seems that around 1990 the field of surface plasmons turned more towards applications and started to expand and penetrate into various interdisciplinary research fields. One of the factors that led to this upsurge is the close links between surface plasmons and near-field optics and nano-optics. The upsurge is also based on the development of top-down and bottom-up techniques for fabricating metallic nanostructures, such as electron-beam lithography, focused ion beam etching and various chemical synthesis methods. Now, this is a well-established research field, which covers various aspects of surface plasmons towards realization of a variety of surface plasmon based devices such as sensors, plasmonic waveguides, plasmonic light emitting devices, plasmonic solar cells, etc.

1.1.1 Plasmons or plasma oscillations

There is a dense assembly of negatively charged free electrons inside a conductor. The free electron charge density is 10^{28} m^{-3} and therefore, the group of free electrons can be compared with a plasma of particles. There is also an equally charged positive ion lattice inside a conductor. Since, positive ions have an infinitely large mass compared with these free electrons, therefore, these positive ions can be represented by a positive constant background. However, the total charge density inside the conductor still remains to be zero. If the density of free electrons is locally reduced by applying an external field on the conductor so that the movement of free electrons may take place, then the negative free electrons are no longer screened by the background and the neutrality of the charge density is altered. In this context, the free electrons begin to get attracted by the positive ion background. This attraction acts as a driving force for free electrons and they move to positive region and accumulate with a density greater than necessary to obtain charge neutrality. Now, at this point, the coulomb repulsion among the moving free electrons acts as a restoring force and produces motion in opposite direction. The resultant of the two forces (i.e., attractive driving force and repulsive restoring force) set up the longitudinal

oscillations among the free electrons. These oscillations are known as plasma oscillations and a plasmon is a quantum of the plasma oscillations.

1.1.2 Surface plasmon polaritons (SPPs)

Surface plasmon polaritons (SPPs) which is also named interchangeably as surface plasmon wave are surface modes that propagate at metal-dielectric interfaces and constitute an electromagnetic field coupled to oscillations of the conduction electrons at the metal surface as shown in Fig. 1.1 [3]. These oscillations get excited when the energy and wave-vector of incident light at the interface becomes equal to that of surface plasmon modes supported by the interface. As a result of these oscillations, under the action of the rapidly changing electromagnetic field, a wave, called surface plasmon wave, gets generated, which travels along the interface and its field amplitude decays exponentially in both the metal and the dielectric medium as given in Fig. 1.2 and Fig. 1.3. It can be observed in

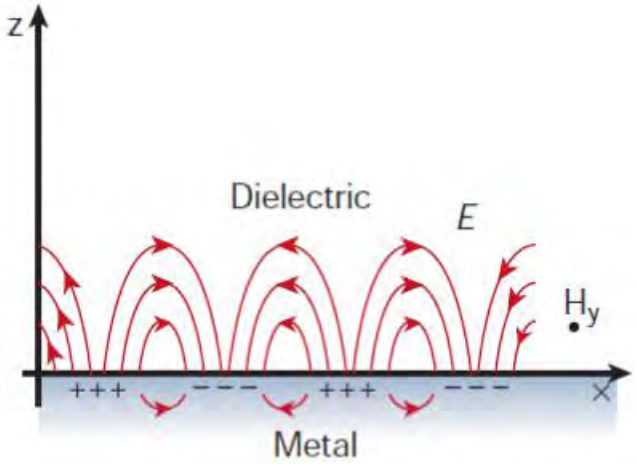

Fig. 1.1 The surface charge and electromagnetic field of the SPPs propagating on a surface in the x direction [3].

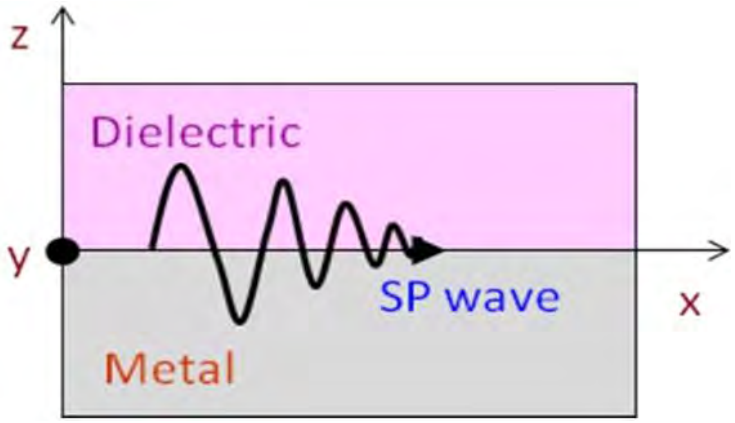

Fig. 1.2 Schematic of surface plasmon wave at a metal-dielectric interface.

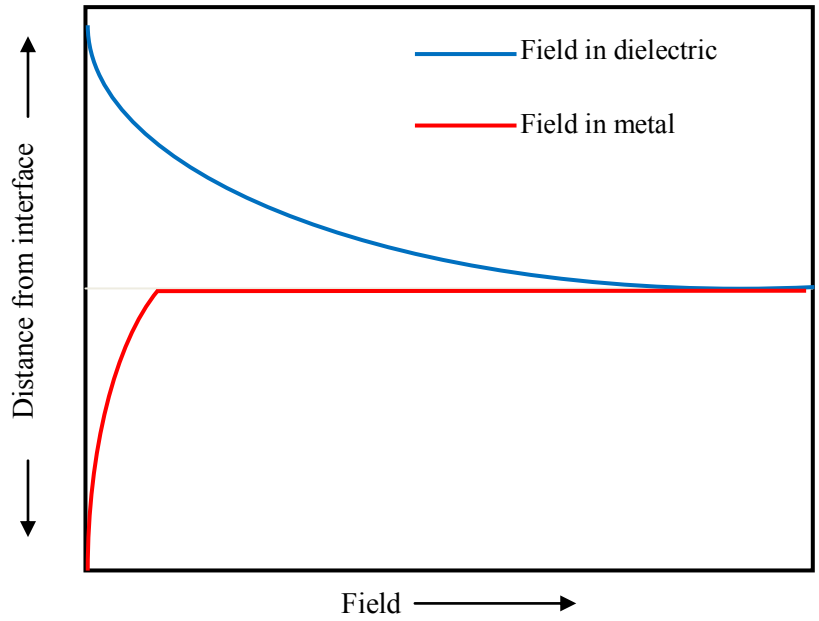

Fig. 1.3 Variation of the field of surface plasmon wave across the metal-dielectric interface.

Fig. 1.3 that the decay of field amplitude in metal is faster than that in the dielectric medium. This can be attributed to the imaginary part of the metal dielectric function. Also, these waves are transverse magnetically (TM) polarized and get excited by only TM polarized light. Due to this exponential decay of field intensity, the field has its maximum at metal-dielectric interface itself. Both of these crucial properties of surface plasmons being TM-polarized and exponential decay of electric field are found by solving the Maxwell's equation for metal-dielectric kind of refractive index distribution. By the solution of Maxwell's equation, one can also show that the surface plasmon wave propagation constant (k_{sp}) is continues through the metal-dielectric interface and is given by

$$k_{sp} = \frac{\omega}{c}\left(\frac{\varepsilon_m \varepsilon_s}{\varepsilon_m + \varepsilon_s}\right)^{1/2}, \tag{1.1}$$

where ε_m and ε_s represent the dielectric constants of metal layer and the dielectric medium; ω represents the frequency of incident light, and c is the velocity of light. The above equation implies that the properties of surface plasmon wave vector depend on both media, i.e., metal and dielectric. The derivation of surface plasmon wave propagation constant k_{sp} of Eqn. (1.1) is given in chapter 3.

1.2 Excitation of surface plasmons

The maximum propagation constant of the light wave at frequency ω propagating through the dielectric medium is given by

$$k_s = \frac{\omega}{c}\sqrt{\varepsilon_s} \quad (1.2)$$

Since $\varepsilon_m < 0$ (i.e., for metal) and $\varepsilon_s > 0$ (i.e., for dielectric), for a given frequency, the propagation constant of surface plasmon is greater than that of the light wave (of same polarization state as that of the surface plasmon wave, i.e., p-polarized) in dielectric medium as illustrated in Fig. 1.4. Dotted straight line in Fig. 1.4 corresponds to light line following the dispersion relation ω = ck and the solid curve corresponds to surface plasmons bound to the interface. It can be observed that for a light wave of frequency ω_o, the wave vector of surface plasmon is greater than that of light. Hence, the light directly incident from the dielectric medium at the metal dielectric interface cannot excite surface plasmons [4]. Therefore, to excite surface plasmons, the momentum and hence the wave vector of the exciting light in dielectric medium should be increased. In other words, an extra momentum (and energy) must be imparted to light wave in order to get the surface plasmons excited at a metal-dielectric interface. There are special techniques for the excitation of surface plasmons at a metal-dielectric interface, in which the wave vector of the incident light is increased to match with surface plasmons. Two most general techniques are named as Otto and Kretschmann-Raether configurations. Some periodically structured surfaces have also been used for increasing the wave vector of the incident light.

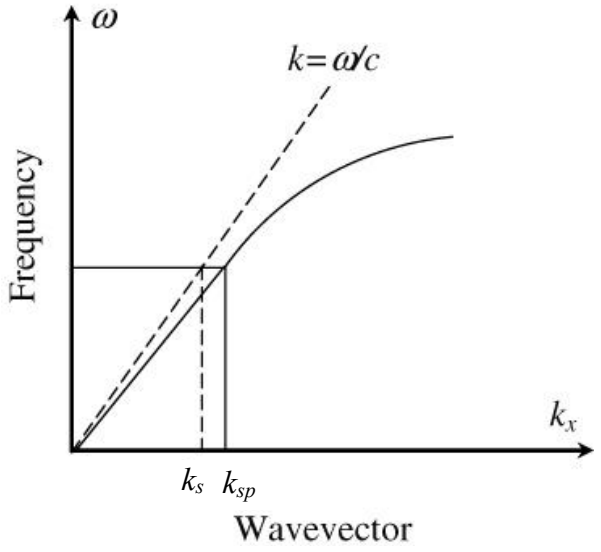

Fig. 1.4 Dispersion curves for surface plasmon wave (k_{sp}) and the direct light incident through the dielectric medium (k_s).

1.2.1 Otto configuration

The general idea behind this configuration was the coupling of surface plasmon wave with the evanescent wave, which is set up due to attenuated total internal reflection (ATR) at the base of a coupling prism when a light beam is incident at an angle greater than the critical angle (θ_{ATR}) at prism-air interface [5]-[6]. Fig. 1.5 exhibits the setting up of an evanescent wave. The nature of evanescent wave (an exponentially decaying wave propagating along the interface of two media due to the occurrence of total internal reflection) is known to have the propagation constant along the interface and to decay exponentially in the dielectric medium adjacent to metal layer. Both of these characteristics of evanescent wave

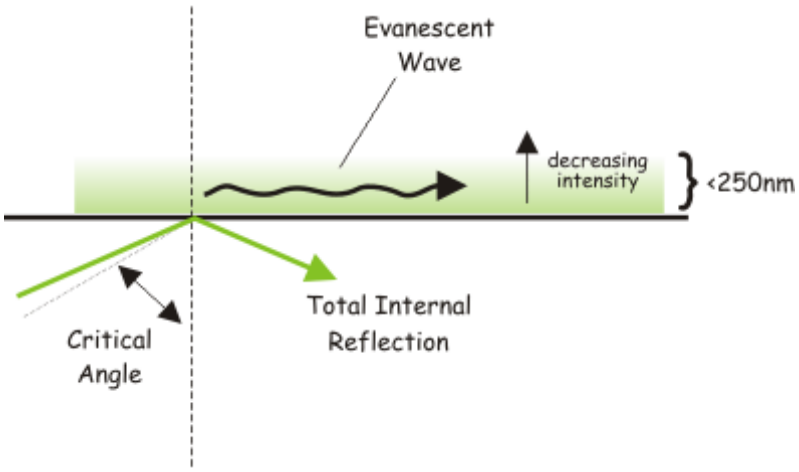

Fig. 1.5 Illustration of setting up of an evanescent wave at prism-metal interface at $\theta > \theta_{ATR}$.

are similar to those of a surface plasmon wave, therefore, there is a strong possibility of interaction between these waves. The x-component of the wave propagation constant of the evanescent wave at prism-air interface is given by

$$k_{ev} = k_p \, sin\theta = \frac{\omega}{c}\sqrt{\varepsilon_p} \, sin\theta. \tag{1.3}$$

If a metal surface is now brought in contact of this decaying evanescent field in such a way that an air gap remains between the prism base and metal layer, then the evanescent field at prism-air interface can excite the surface plasmons at the air-metal interface as shown in Fig. 1.6. However, this configuration is difficult to realize practically as the metal has to be brought within around 200 nm of the prism surface, because the effect of evanescent field beyond 200 nm from the prism surface has very negligible effect on excitation of surface plasmon wave. This approach has been found to be very useful in studying the single-crystal metal surfaces.

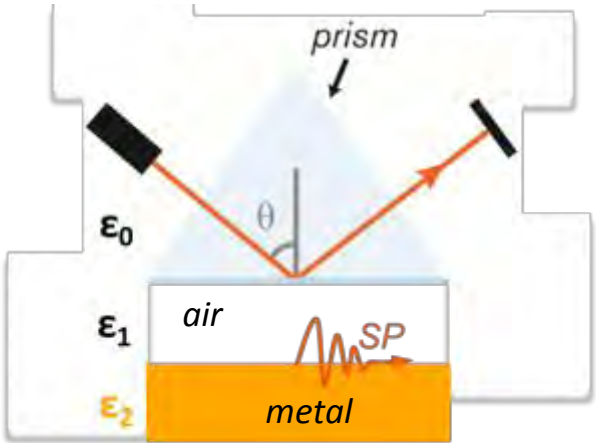

Fig. 1.6 Otto configuration for the excitation of surface plasmons at metal-dielectric interface.

1.2.2 Kretschmann–Raether configuration

As a significant improvement to Otto configuration, Kretschmann and Raether realized that the metal layer could be used as the spacing layer, i.e., evanescent wave generated at the prism-metal layer interface can excite surface plasmons at the metal-air interface so long as the metal layer thickness is not too large. They devised a new configuration [7], given in Fig. 1.7. In this configuration as well, surface plasmons are excited by an evanescent wave from a high refractive index glass prism at ATR condition. However, unlike Otto configuration, the base of the glass prism is coated with a thin metal film (typically around 50 nm thick) and is kept in direct contact with the dielectric medium of lower refractive index (such as air or some other dielectric sample). When a p-polarized light beam is incident through the prism on the prism-metal layer interface at an angle θ equal to or greater than the angle required for ATR (θ_{ATR}), the evanescent wave is generated at the prism-metal layer interface. Fig. 1.8 shows the dispersion curves of the surface plasmon

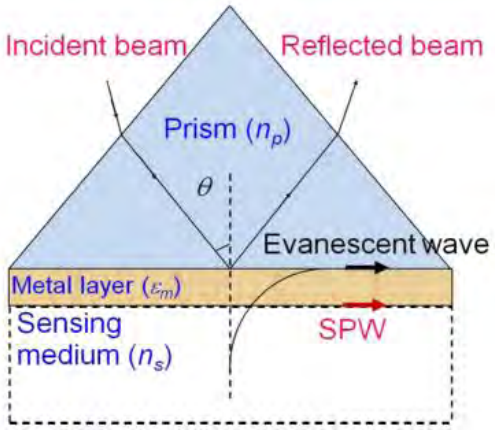

Fig. 1.7 Kretschmann-Raether configuration for the excitation of surface plasmons at metal-dielectric interface.

along with those of the direct light and the light incident through a glass prism of higher refractive index. The wave vector k_{ev} of the evanescent wave, corresponding to incident angle, is equal to the lateral component of the wave vector of the incident light in the prism, as given in Eqn. (1.3). The excitation of surface plasmon occurs when the wave vector of the propagation constant of evanescent wave exactly matches with that of the surface plasmon of similar frequency and state of polarization. This occurs at a particular angle of incidence θ_{res} and by equating Eqn. (1.1) and Eqn. (1.3), the corresponding resonance condition for surface plasmons is given as

$$\frac{\omega}{c}\sqrt{\varepsilon_p}\ sin\,\theta_{res} = \frac{\omega}{c}\left(\frac{\varepsilon_m \varepsilon_s}{\varepsilon_m + \varepsilon_s}\right)^{1/2}. \tag{1.4}$$

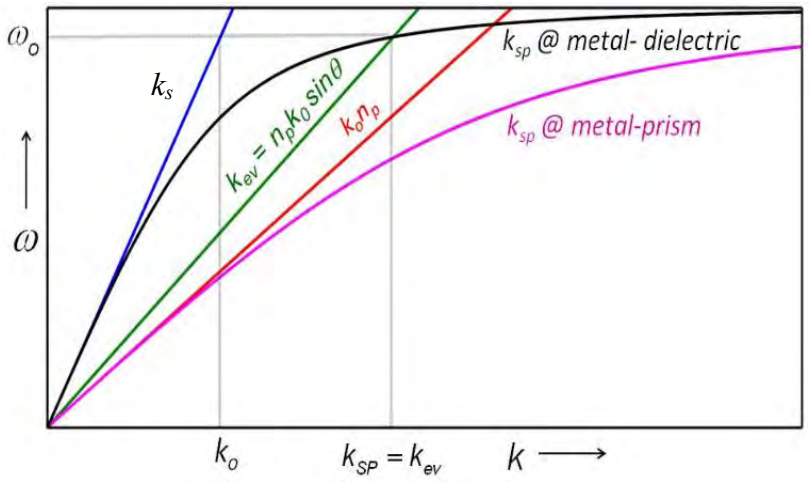

Fig. 1.8 Dispersion curves for direct light wave in dielectric (k_s), evanescent wave (k_{ev}) for $k_{ev} = k_p$ and $k_{ev} = n_p k_o \sin\theta$, surface plasmon wave k_{sp} at metal-dielectric interface and at metal-prism interface.

Fig. 1.8 clearly shows that the propagation constant curves corresponding to surface plasmon wave and evanescent wave cross each other at many positions lying between $k_{ev} = n_p k_o \sin\theta$ and $k_{ev} = k_p$ where $k_p = n_p k_o$ [i.e., for different sets of angle of incidence and frequency (θ, ω)]. This implies that the propagation constant of evanescent wave (k_{ev}) may match with that of the surface plasmon wave at the metal-dielectric interface depending on the frequency and angle of incidence of light beam. As a very important observation, the surface plasmon wave propagation constant for metal-prism interface lies to right of the maximum propagation constant of evanescent wave (k_{ev}=k_p), and the two curves never cross each other. This suggests that, in this configuration, there is no excitation of surface plasmons at metal-prism interface. In this configuration, if we keep the incident angle fixed and light of varying wavelength is used, then the resonance happens for a particular wavelength of light. In that case θ_{res} is being replaced by λ_{res} in Eqn. (1.4) and we get the resonance condition as

$$\frac{\omega}{c}\sqrt{\varepsilon_p}\ sin\,\lambda_{res} = \frac{\omega}{c}\left(\frac{\varepsilon_m \varepsilon_s}{\varepsilon_m + \varepsilon_s}\right)^{1/2}. \quad (1.5)$$

1.3 Surface plasmon resonance (SPR)

Surface plasmon resonance (SPR) is an optical phenomenon in which a p-polarized light beam satisfies the resonance condition and excites a charge density oscillation known as SPP which propagates along the metal-dielectric interface. The condition of resonance and the requirements for the excitation of SPP are discussed in subsection 1.2.1 and 1.2.2. The terms SPP and SPR are very closely related, but there is subtle difference between them. SPR is the phenomenon of resonance i.e matching of the wavevectors between incident light and surface modes and SPP is the outcome of the phenomenon of resonance. The resonance condition explicitly depends on the incident angle, wavelength of the light beam and the dielectric constant of both the metal as well as the dielectric. The resonance can happen in particular angle of incidence for fixed wavelength of light and alternately can happen at particular wavelength of light for fixed angle of incidence. When the incidence angle is varied, it is called angular interrogation method and when the wavelength of incident light is varied it is called wavelength interrogation method. The after effect of the resonance appears as a sharp dip (loss) of output optical signal because of the shift of power from the incident light to surface modes. The excited SPPs are very sensitive to the adjacent environment. Any change in refractive index near the metal-dielectric interface causes a change in SPPs which results a change in the value of resonance parameters and consequently changes the output optical signal. So, by detecting the change in the output optical signal, corresponding change in the refractive index of the dielectric material can be detected. This is how SPR phenomenon contributes is sensing. SPR sensor allows label free detection and online monitoring, so no cumbersome post processing is required for effective detection. Instead of prism, the use of optical fiber and PCF in implementing SPR sensor has added more advantages like miniaturization, remote sensing, enhanced sensitivity and so on. A simplified schematic setup of prism based SPR sensor is shown in

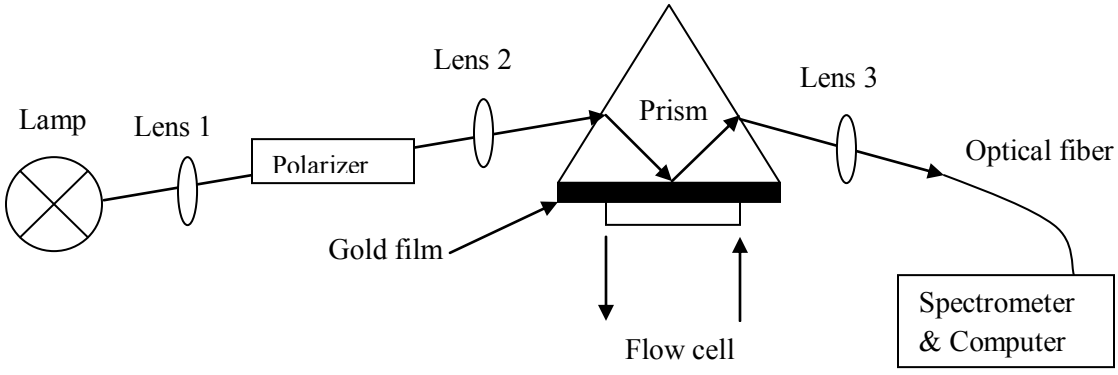

Fig. 1.9 Simplified schematic setup of prism based SPR sensor. For optical fiber or PCF based configuration, prism will be replaced by optical fiber or PCF.

Fig.1.9. Here P-polarized light is incident on prism in an angle greater than the critical angle. At certain angle, resonance between incident light and surface mode happens and power is shifted from incident light to surface mode. Consequently, output power dip loss is resulted at resonance and detected in spectrometer and computer. For this method, sensing is accomplished using Eqn. 1.4. Inlet and outlet of flow cell controls the flow of sensing medium.

1.4 SPR sensing techniques

The work of Otto [5]-[6] and later by Kretschmann and Raether [7] in the late 1960s brought understanding about the practical application of SPR technique and showed the versatility of this phenomenon. Soon the advantage of using optical fiber over prism based configuration brought the attention of researcher in implementing the SPR sensing technique with optical fiber. The inception of PCF with inherent design flexibility and versatility over optical fiber made it a lucrative alternative for the design and implementation of SPR sensing system. With the enormous design possibilities of light guiding in micro structured optical fiber or namely PCF, the SPR sensing research community has come up with numerous configurations and probe designs.

Most of the realized fiber-based SPR sensors work in the transmission regime where light from a broadband source is launched into one end of the fiber and is detected at the other end. This configuration is shown in Fig. 1.10. Excitation of SPR in optical fiber is similar to the excitation of SPR in the prism configuration. Light propagating in the fiber also experience TIR at the core-cladding interface. In a portion of the fiber, cladding is removed and a thin metal layer of typically 40 nm is deposited on the cleaved portion of the fiber. This metal layer remains in contact with the medium to be sensed. Upon meeting the light launching condition, TIR happens and SPR phenomenon occurs. Similarity between light propagation in the optical fiber via TIR and in prism configuration has led to many successful attempts to realize SPR sensors in optical fibers.

SPR fiber sensors can also work in the reflection regime (fiber probe) as an alternative to the transmission regime. Fig. 1.11 shows a sensor consisting of the fiber with a perfect cleave and a layer of gold or another reflecting material at one end of the fiber which reflects light back towards the detector at the opposite end. Light propagating in the fiber is being altered by coupling to the surface plasmon if SPR occurs. The reflected light from the cleaved side is detected when travelling back. The design of the probe allows the sensor to be extremely compact, user-friendly and practical for *in situ* measurements in small spatial volumes.

It is possible to use a two-dimensional photonic crystal as a fiber cladding, by choosing a core material with a higher refractive index than the cladding effective index. An example

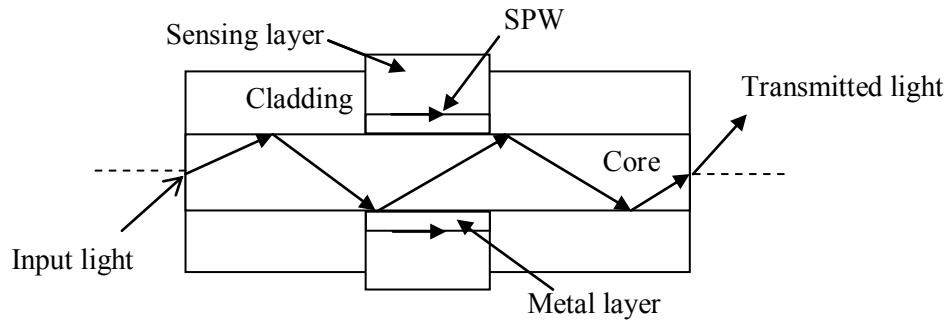

Fig. 1.10 Schematic lateral cross section of a typical probe of optical fiber based SPR sensor.

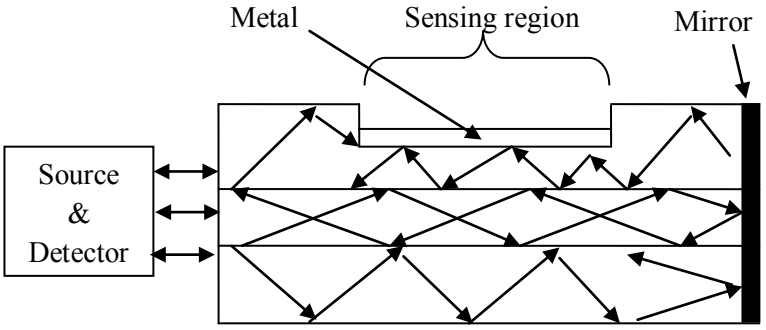

Fig. 1.11 Diagram showing optical fiber based SPR sensors working in the reflection regime.

of this kind of structures is the PCF with a solid silica core surrounded by a photonic crystal cladding with a hexagonal lattice of air-holes is shown in Fig. 1.12. Different geometry and different materials will imply different structural design to enable different guidance mechanisms through the PCFs namely modified TIR and/or PBG guidance. As an example, a conventional hexagonal lattice PCF, modified to form multiple sensing channels which are coated by metal layer to generate evanescent field is shown in Fig. 1.13 [8]. Here, the light is guided through the core and the Gaussian-like leaky mode of PCF generates evanescent filed upon incident on metal layer. This evanescent wave is used to excite SPPs in the metal-analyte boundary of analyte channels. Like optical fiber, here also evanescent filed penetrates through the gold and excites surface plasmons in gold-analyte boundary. Through the interaction of surface plasmons and analyte, sensing is accomplished.

One approach in the excitation of SPR for chemical/bio sensing is to provide the fiber end with a suitable indicator or a material that responds to the parameter of interest. Chemically sensitive thin films deposited on selected areas of PCF can influence the propagation of light in such fibers depending on the presence or absence of chemical/biological molecules in the surrounding environment. A wide range of PCF based SPR sensors have been

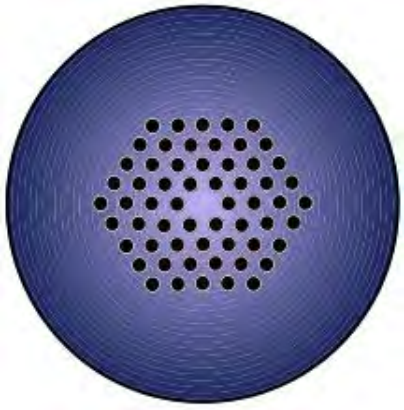

Fig. 1.12 A frequently used hexagonal lattice solid-core PCF design.

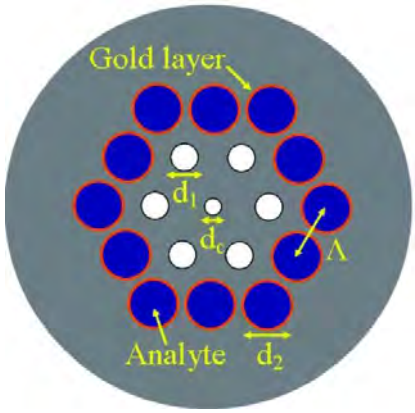

Fig. 1.13 Schematic of multiple analyte channel PCF for excitation of SPR [8].

developed for selective biomolecule detection. Another approach for chemical/ biochemical sensing is to utilize the ability of the PCF to accommodate biological and chemical samples in gaseous or liquid forms in the immediate vicinity of the fiber core or even inside the core. PCFs can be used simultaneously for light guiding and as fluidic channel, leading to a strong light/sample overlap. Due to PCFs diversity of features they introduce a large number of new and improved applications in the fiber optic sensing domain.

1.5 Motivation

In the last two decades, the over pressing need for faster and improved means of detection, communication and data processing has encouraged the rapid growth of all-optical components in the field of sensing. This has led to the development of a variety of new optical sensing devices which are able to detect, measure, and process data using electromagnetic radiation. In addition, materials technology and fabrication methods, particularly for semiconductors, have advanced, allowing devices to be built with fine

structural details. In combination, these developments have brought technology to a point that new applications can be envisaged, where all-optical sensing components and circuits are replacing conventional mechanical and electrical sensors.

The motivation behind research and development activities in optical sensing relies on the expectation that properties of the optical sensing field are significantly advantageous over conventional sensing. In fact optical fibers has revolutionized different fields such as telecommunications and sensing, leading to the creation of high sensitivity and controlled systems based on light guidance. The remarkable characteristics of fiber optics such as geometric versatility, increased sensitivity over existing techniques and inherent compatibility with fiber optic telecommunications technology make them stand out for sensing applications. Optical-fibers-based sensors are low cost and efficient solutions for several industries due to their high sensitivity, small size, robustness, flexibility and ability for remote monitoring as well as multiplexing [9]. Other advantages entail their aptitude to be used even in the presence of unfavorable environmental conditions such as noise, strong electromagnetic fields, high voltages, nuclear radiation, explosive or chemically corrosive media and high temperatures among others.

In this context, SPR based sensing possesses the majority of these advantages. The main reason for SPR sensors to become a powerful tool is the characterization of real-time monitoring and label-free sensing with high detection sensitivity and wide dynamic range. The conventional excitation of surface plasmons using a prism requires a very sophisticated and bulky experimental setup. Their large detection spot and the need of a coupling prism limit their effectiveness for probing nanovolumes and single cells. For example, a commercial SPR system from BIAcore [10] has a price of several hundred thousand US dollars, and weighs over 40 kg. To eliminate the inherent difficulties involved in the prism based SPR system, optical fiber based sensing system has evolved. Later, the inception of PCF with better design flexibility and unprecedented advantages over conventional optical fiber, led the use of PCF in SPR sensing system. These overriding advantages of PCF are the motivation behind this work.

1.6 Scope of the thesis

This dissertation explores an exciting approach of integrating square lattice PCF (SL-PCF) for SPR sensing application. The primary aim of this investigation is to exploit square lattice structure of PCF along with different design considerations for enhanced performance of SPR sensor in refractive index sensing.

This dissertation is arranged in the following manner: chapter one (this chapter) delineates the pivotal concepts of SPR sensing. The condition and requirements for the excitation of surface plasmons is discussed in this chapter. Different techniques of SPR sensing and

motivation behind this work is also touched upon in this chapter. Review of literature on optical fiber and PCF based SPR sensor and objectives of this thesis are presented in chapter two. Optical properties of metals are discussed in chapter three. The excitation of SPPs on planar metal surface and on metallic solid wire is investigated in this chapter. Different performance parameters of SPR sensor are also introduced in this chapter. In chapter four, step by step modeling technique, simulation, data acquisition, analysis and outcome is discussed to obtain some useful findings in performance enhancement and quantification of PCF based SPR sensor. Finally, chapter five contains the concluding remarks and some light on the future endeavor.

CHAPTER 2

REVIEW OF SPR SENSORS AND OBJECTIVES OF THE THESIS

Though the initiation of using SPR technique for sensing application started with the investigation of Otto in 1968 [5]-[6], the actual adoption of SPR technique for sensing application started with the Kretschmann configuration proposed in 1971 [7]. The ATR method has proven to be extremely sensitive to various changes at metal surfaces and is now used as an indispensable tool for sensing. The initial investigation of SPR sensor started with prism based configuration and we can find this configuration in commercial SPR sensor. As the ATR phenomenon can be materialized in optical fiber also, the need of miniaturization, remote sensing, high degree of integration and so on led to numerous investigation of optical fiber based SPR sensors. Over the period of time, numerous optical fiber based configuration both in transmission and reflection regime has been investigated. Later, the inception of PCF has intrigued the SPR sensor researching community. The special ability of the PCF to carry light as well as the sensing material through the air hole surely has added new dimension in the design and implementation of the SPR sensor. Many other inherent advantages of PCF over optical fiber has led to numerous investigations of PCF based SPR sensor.

2.1 Prism based configuration

The use of prism couplers to couple light to SPs is straightforward, versatile, and does not require complex optical instrumentation. Therefore, SPR sensors based ATR method and prism couplers have been the most widely used. All major types of modulation have been implemented in prism-based SPR sensors. In SPR sensors based on spectroscopy of SPs, the angular or wavelength spectrum of the optical wave coupled with the SP is measured. Alternatively, changes in the intensity or phase of the reflected wave can be measured at a fixed wavelength and an angle of incidence. While the spectroscopic SPR sensors usually offer higher resolution, they provide a rather limited number of sensing channels. By contrast, intensity or phase modulations can be adopted by SPR imaging configurations, where independent measurements are performed in as many as hundreds of sensing channels simultaneously. Over the period of time, numerous prism based SPR sensor configurations have been investigated and tested in the lab [11]. Successful implementation has resulted in the commercialization of many SPR sensing system. But in many cases prism based SPR sensor setup is very costly and bulky in size. Though the prism based commercial sensors are available in the market, for the disadvantages in prism based SPR sensing systems, we have focused on the waveguide based SPR sensing system in our investigation. So, elaborate discussion on the chronological development with sufficient details in prism based SPR sensing system is beyond the scope of this thesis and is not discussed here.

2.2 Optical fiber based SPR sensors

Among the first few reports on fiber optic SPR sensors, the work reported by Villuendas and Palayo got attention of researchers [12]. Their work consisted of experimental results on aqueous sucrose solutions for sensitivity and dynamic range evaluation. Soon after, a four layer fiber optic SPR sensor was reported with enhanced sensitivity and dynamic range. Around the same time, a single mode optical fiber SPR sensor with SPR excitation on the tip was reported. Among these reports, the one reported by Jorgenson and Yee got the most attention, due to a complete theoretical and experimental study of fiber optic SPR sensors, with an application in chemical sensing [12]. Jorgenson and Yee replaced the prism of the Kretschmann configuration by the core of an optical fiber and excited surface plasmons by the evanescent field at the core-cladding interface. Their sensor was well accepted because SPR sensors utilizing optical fibers have been found to provide multiple advantages over prism based sensors. These sensors are simple in design, miniaturized, low cost, highly sensitive and accurate. Use of optical fiber further adds the advantage of online monitoring, remote sensing and freedom from electric shocks and electromagnetic interferences. The compatibility of gold with various biological species and functional groups makes these sensors useful for biosensing applications. Since then, various fiber optic sensors have been reported [13]. A number of attempts have been made to enhance the sensitivity of these sensors by various probe designs and additional layers [14]. Later, a fiber-optic SPR sensor based on spectral interrogation in a side polished single-mode fiber using depolarized light was reported [15] as shown in Fig. 2.1. These sensors have been employed in sensing of different chemicals and biochemicals and environmental and health monitoring [16]. A new approach of hetero-core structure for a fiber-optic SPR sensor was introduced [17]. The hetero-core structured fiber-optic SPR probe consists of two fibers with different core diameter connected by thermal fusion splicing as shown in Fig. 2.2. This was done, deliberately, to leak the transmitted power into the cladding layer of small core diameter fiber so that the leaked light may induce an optical evanescent wave required for SPR excitation. Application of D-type optical fiber sensor, as shown in Fig. 2.3, has also been a very interesting addition to the fiber-optic SPR sensor technology [18]. Nano particles films have also been used to enhance the performance of SPR sensor [19]. A schematic is shown in Fig. 2.4. Some theoretical reports have presented the collaboration of plasmonic structures with fiber Bragg gratings and long period gratings [20]. However, the SPR based fiber Bragg gratings sensors have not yet been realized probably due to experimental difficulties and still optimization of certain parameters is required before fabrication. The fiber optic interferometric sensors utilizing SPR have also been studied in Fabry-Perot configuration [21]. In Table 2.1, the performance parameters of a variety of optical fibre based SPR sensors documented in the literature is given.

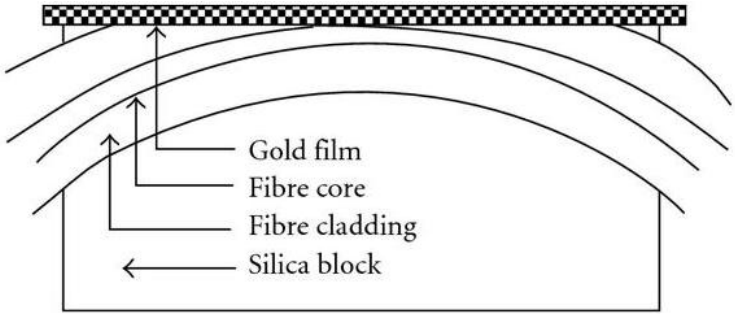

Fig. 2.1 Schematic of an SPR sensor using side-polished single-mode optical fiber [15].

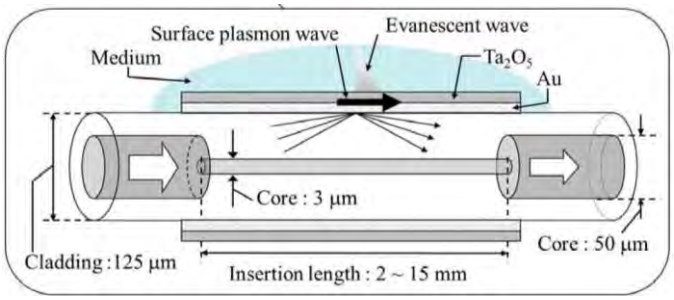

Fig. 2.2 Hetero-core structured optical fiber sensor, with the gold layer of 50 nm thickness on the cladding surface of the single mode fiber [17].

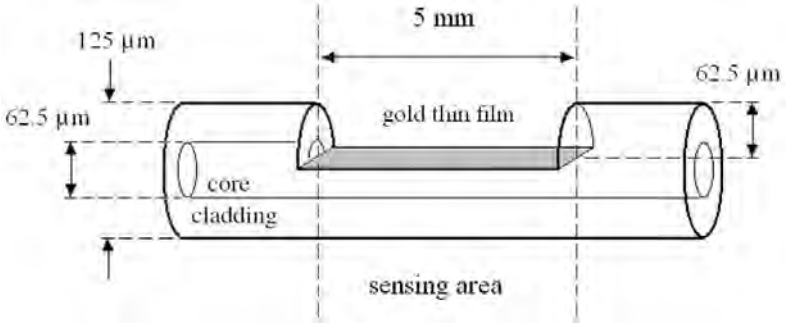

Fig. 2.3 D-type optical fiber SPR sensor probe [18].

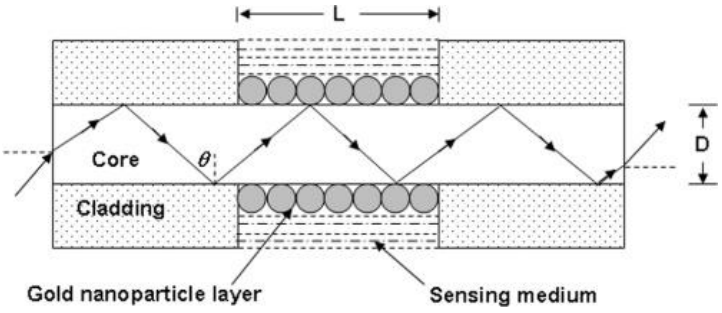

Fig. 2.4 A fiber-optic SPR sensor with metal nanoparticle layers [19].

Table 2.1 Performance parameters of various optical fiber refractive index sensors.

Sensor Type	Detection Range (RI)	Sensitivity (nm/RIU)	Ref.
SPR MMF –Au-Ag alloy nanoparticle	~1.342-1.346	~3000	[19]
MMF – modified end face	~1.33-1.376	~533	[22]
FBG – tilted grating, Au coating	~1.3-1.38	~3365	[23]
LPG – 3μm planar, Au coating	~1.329-1.340	~1100	[24]
MMF – Tapered, Au coating	~1.333-1.343	~2700-4900	[25]
MMF – flat tip, Ag mirror, SiO layer	~1.3365-1.4126	~3800	[26]
SPR MMF - cladding removed, Au coating, surface roughness	~ 1.3335-1.4018	~1600-3000	[27]

2.3 PCF based SPR sensors

In the realm of optical fiber sensing, PCF offers a high degree of freedom in design flexibility, facilitating the development of new sensing configurations. The sensing mechanism of index-guiding PCF sensors is also based on the evanescent interaction between the guided optical field and the sample, akin to that in the conventional sensors. The schematic illustration of the active sensing regions around the core of index guiding PCF is shown in Fig 2.5. However, they do not require cumbersome post processing procedures, since the presence of air-holes in the cladding microstructure allows the accommodation of biological and chemical samples in gaseous or liquid forms in the immediate vicinity of the fiber core. In addition, PCFs naturally integrate optical detection with microfluidics, allowing for continuous on-line monitoring of samples in real-time. The

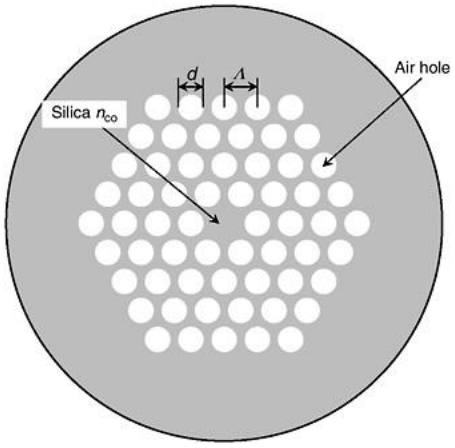

Fig. 2.5 Schematic illustration of the active sensing regions around the core of an index-guiding PCF.

infiltration of sample into the PCF cladding holes also allows the fiber to maintain its original structure, without the need to even remove the polymer coating of the fiber. Consequently the index-guiding PCF provides superior structural robustness compared to the conventional fiber sensors. The evanescent-wave PCF sensor configuration was first theoretically and numerically studied by Monro et al. [28]. In principle, strong light-matter interaction requires a significant modal power overlap with the fiber holes within the wavelength range. The power overlap decreases with core size and increases with wavelength, as light of longer wavelength is less tightly confined in the solid core of the index-guiding PCF. Therefore, a larger fraction of the guided mode extends into the cladding holes. The first experimental demonstration of evanescent-wave gas detection with index-guiding PCF was reported in 2002 [29]. The fiber used had a relatively low power overlap (~5.5% at 1530 nm) of the optical field with the sample. Several approaches have been reported in order to improve sensitivity of PCF sensors. For example, dual-cladding PCF in which the solid fiber core was fabricated with additional holes to increase the interaction of the optical field with the sample (e.g. from 0.041% to 4.22% at 633 nm for a water-filled fiber [30]). The relatively simple concept of suspended-core fiber in which a small core is held in air by three thin silica struts was introduced. These fibers have demonstrated large modal overlap of 29% at 1550 nm, which can find useful applications in SPR based sensing [31]. In addition to chemical sensing, index guiding PCF based SPR sensor configuration has also been applied to biosensing, whereby fluorescently labeled antibodies in aqueous solution were detected via absorption spectroscopy [32].

Hollow core PCF exhibit a significant advantage for sensing applications over evanescent wave PCF sensors in that the modal overlap with the sample is considerably improved, guiding more than 90% of the power in the core defect of the fiber. The schematic illustration of the active sensing regions around the core of index guiding PCF is shown in Fig 2.6. Consequently, the strong light confinement provided by the photonic band gap

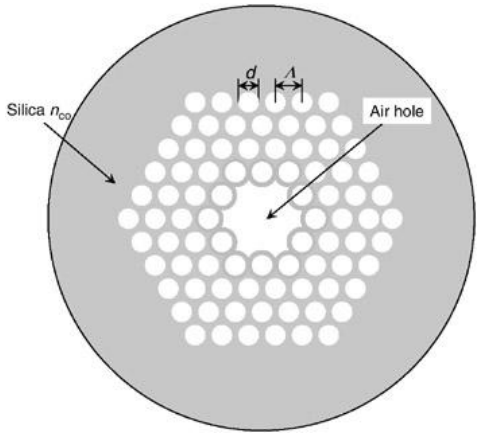

Fig. 2.6 Schematic illustration of the active sensing regions around the core of a hollow-core PBG-PCF.

(PBG) and the possibility of tuning the PBG by tailoring the structural parameters have attracted much attention in the field of fiber sensors. It has been shown that the hollow core of the PBG-PCF selectively filled with a dye solution achieved an almost 100% modal overlap with the sample material, surpassing the performance of index-guiding PCFs [33]. In particular, the detection limit of fluorescence sensing was demonstrated to improve by four orders of magnitude. The study of fluid sensing characteristics using PBG-PCF has been performed in [34]. The results obtained demonstrated that effective sensing in HC-PCF is feasible using low-power, cost-effective light sources to realize miniaturization of the system setup.

In recent times, SPR sensors based on modified structure of photonic crystal waveguide [35] has been proposed. In the photonic crystal waveguide based SPR sensor, plasmons on a surface of a thin metal film are excited by a Gaussian-like leaky mode of an effectively single-mode photonic crystal waveguide. It has been demonstrated that effective refractive index of a waveguide core mode can be designed to be considerably smaller than that of a core material, enabling efficient phase matching with plasmons at any wavelength of choice, while retaining highly sensitive response to changes in the refractive index of an analyte layer. This is quite an ideal technique for the development of portable SPR biochemical sensors. As another crucial advancement, the concept of a microstructured optical fiber-based SPR sensor with optimized microfluidics is proposed [8], [36], schematic of which is given in Fig. 2.7. In this design, plasmons on the inner surface of large metallized channels containing analyte can be excited by a fundamental mode of a single-mode microstructured fiber. Phase matching between plasmon and a core mode is enforced by introducing air filled microstructure into the fiber core, thus allowing tuning of the modal refractive index and its matching with that of a plasmon. Sensitivity studies show that refractive index changes of RIU leads to easily detectable 1% change in the transmitted light intensity.

Multi analyte channel PCF based SPR sensor was investigated by Gauvreau et al. in [37], where to enhance the flow of microfluidics, multiples analyte channel was used as shown in Fig. 2.8. But it necessitates the use of more gold coating in the multiple analyte channels and there was co-channel interference from the neighbouring analyte channel. To eliminate all these disadvantages, Binbin Shuai et al. propose a PCF based SPR sensor with multiple core and with only one analyte channel as shown in Fig. 2.8 [38]. Again in an investigation Binbin Shuai et al. has proposed a PCF structure with liquid filled multiple core and single analyte channel [39] based SPR sensor, schematic cross section of which is shown in Fig. 2.9. Documented performance parameters of few recent PCF based SPR sensor is given in Table 2.2.

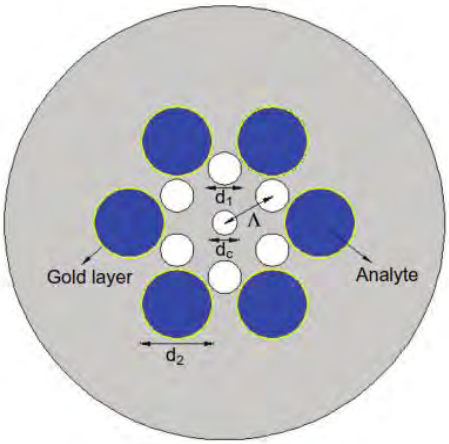

Fig. 2.7 Micrstructured optical fiber based SPR sensor [36].

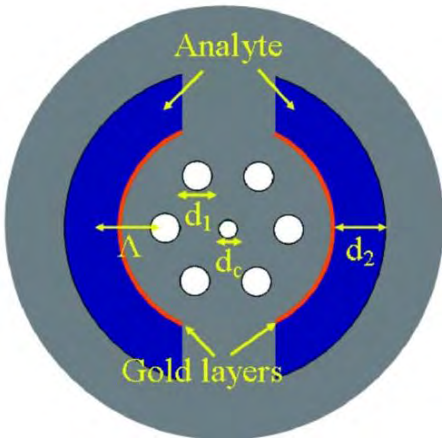

Fig. 2.8 Depiction of multi analyte channel PCF based surface plasmon resonance sensor [37].

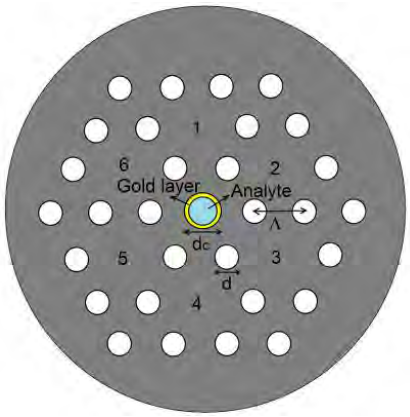

Fig. 2.9 Schematic of the proposed PCF based SPR sensor with multiple core and single analyte channel [38].

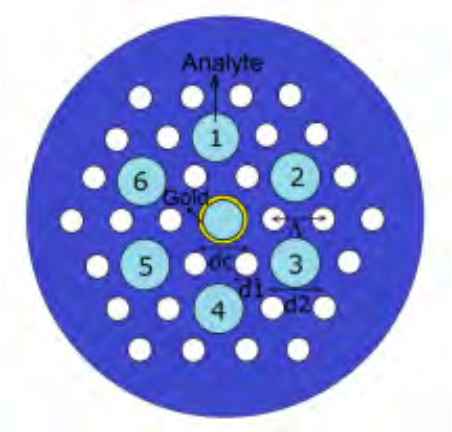

Fig. 2.10 Liquid core PCF based SPR sensor with single analyte channel [39].

Table 2.2 Performance parameters of few recently proposed PCF based SPR sensor.

Optical structure	Detection RI Range (RIU)	Wavelength of operation (nm)	Average Sensitivity (nm/RIU)	Ref.
Hexagonal lattice Solid core, MCHF	1.33-1.42	400-800	2929.39	[38]
	1.43-1.53	800-1850	9231.27	[38]
Liquid core, MCHF	1.50-1.53	700-1500	~5500	[39]
Analyte-filled core, HF	1.33-1.42	550-900	2775	[40]
Air hole in core. HF	1.33-1.41	500-850	2728	[41]

2.4 Objectives of the thesis

The primary objective of this thesis is to improve the performance parameters of PCF based SPR sensors. In doing so, the suitability of the SL-PCF for SPR based sensing system will be evaluated first. It is understood from the literature review that multiple analyte channel PCF based SPR sensing system has some disadvantages like more gold consumption in analyte channel coating, co-channel interference from neighboring channels and requirement of more amount of sample for accurate sensing. To eliminate these disadvantages, single analyte channel SPR sensing system will be evaluated which will reduce the gold consumption in analyte channel coating and suppress the co-channel interference. The amount of sample needed for effective detection will also be less. If the coupling between the core guided fundamental mode and plasmonic wave increases, then the sensitivity of the sensor will also increase. To increase the coupling between core

guided fundamental mode and plasmonic wave, multiple cores will be formed in the PCF structure which will increase the overlap between evanescent field and plasmonic wave. As the coupling increases, it will give corresponding rise in sensitivity.

The thickness of the gold coating plays an important role in the penetration of evanescent field and consequently the coupling between core guided mode and plasmonic mode is affected. To observe this effect, thickness of the gold in analyte channel coating will be varied and evaluated. The structure will be further investigated with the use of other metals like silver and copper to evaluate their suitability. The thickness of the silver and copper coating will also be evaluated and compared with that of gold to find their suitability. Gold and silver can be used together in analyte channel coating to utilize the advantage of both the metal. This will be investigated by implementing bimetallic coating of gold and silver to achieve enhanced sensitivity and detection accuracy.

The use of different doping concentration can tune the refractive index in the core of the PCF, which will have corresponding effect in light guidance and coupling. This phenomenon will be utilized and core effective index of PCF will be tuned by using 13.5% GeO_2, 9.1% P_2O_5 and 5.2% B_2O_3 individually. Finally the optimized design parameters and configuration will be evaluated for sensitivity, detection accuracy, dynamic sensing range and detection linearity of the proposed SPR sensor.

Basing on the above design considerations, ultimately this thesis concentrates on achieving enhanced performance of SL-PCF based SPR sensor. This objective will be complemented by the use of multiple core and single analyte channel PCF. Further the objective will be supported by the use of bimetallic analyte channel. Together, with all the analysis and design considerations will yield a PCF based SPR sensor with enhanced performance.

CHAPTER 3

OPTICAL SENSING USING SURFACE PLASMON RESONANCE

The study of light matter interactions plays an important role in understanding our universe and has a long history. When the electromagnetic wave interacts with atoms or molecules, several optical effects may evolve, such as absorption, emission, scattering, refraction, fluorescence, etc. Precise control of the interaction between light and matter becomes the key to create new capabilities of optical devices/instruments for telecommunication, sensing, molecule detection, medical treatment, light source, optical interconnection systems and many other applications.

This chapter provides an introduction to the physics of SPPs. Theory on the properties of propagating SPPs or surface plasmons at a planar metal-dielectric interface by solving Maxwell's equations with the proper boundary conditions is included. Excitation of SPPs on metallic wire and different performance parameters are also described subsequently.

3.1 Optical properties of metals

Metal contains free electrons with concentrations N of the order of 10^{28} m^{-3}. Because of this high electron density, the optical properties of metal mainly depend on the response of the electron ensemble in the conduction band. For metals, the dielectric function and the absorption of light due to the electron transmission to higher energy states can be described by free electron theory of metals. The electron transport in metals is often described by the Drude model, which assumes the metal is a free electron gas [8].

The response of metal to electromagnetic radiation can be defined as

$$\vec{D} = \varepsilon_0 \vec{E} + \vec{P} = \varepsilon_0 \varepsilon(\omega) \vec{E}, \tag{3.1}$$

where $\vec{D}$ is the electric displacement vector, $\vec{E}$ is the electric field, $\vec{P}$ is the electric polarization and ε and ε_0 are the material dependent dielectric permittivity and vacuum dielectric permittivity, respectively. In the free electron model, interactions between electrons are not taken into consideration. The electrons oscillating in response to the applied electromagnetic field are damped via collisions with nuclei at a collision frequency $\gamma = 1/\tau$ where τ is the average time between successive collision. At room temperature, the typical value of τ is in the order of 10^{-14} s, corresponding to $\gamma \sim 10^{14}$ Hz.

Assuming an oscillating electric field

$$\vec{E}(t) = \overrightarrow{E_0} e^{-i\omega t}, \tag{3.2}$$

the motion of the electrons can be described as an oscillation equation

$$m\frac{\partial^2\vec{x}}{\partial t^2}+m\gamma\frac{\partial\vec{x}}{\partial\vec{t}}=-e\overrightarrow{E_0}e^{-i\omega t}, \tag{3.3}$$

where m is the effective mass and e is the electron charge. Eqn. (3.3) has solution of the following form

$$\vec{x}(t)=\frac{e}{m(\omega^2+i\gamma\omega)}\overrightarrow{E_0}e^{-i\omega t}. \tag{3.4}$$

The polarization $\vec{P}$ is then written as:

$$\vec{P}=-Ne\vec{x}=-\frac{e^2N}{m(\omega^2+i\gamma\omega)}\overrightarrow{E_0}e^{-i\omega t} \tag{3.5}$$

$$\text{and } \vec{D}=\varepsilon_0\left(1-\frac{e^2N}{m\varepsilon_0(\omega^2+i\gamma\omega)}\right)\overrightarrow{E_0}e^{-i\omega t}$$

$$=\varepsilon_0\left(1-\frac{{\omega_p}^2}{(\omega^2+i\gamma\omega)}\right)\overrightarrow{E_0}e^{-i\omega t}, \tag{3.6}$$

where ω_p is the oscillation frequency of collective electrons in a volume of metal and is named as plasma frequency, which is defined as

$$\omega_p^2=\frac{e^2N}{\varepsilon_0 m}. \tag{3.7}$$

It is the typical electrostatic oscillation frequency for the electrons to restore around equilibrium positions. Substituting the value of Eqn. (3.1) and Eqn. (3.2) in Eqn. (3.6) the dielectric function can now be expressed by Drude model as

$$\varepsilon(\omega)=1-\frac{\omega_p^2}{\omega^2+i\gamma\omega}. \tag{3.8}$$

With the real and imaginary parts:

$$\varepsilon'(\omega)=1-\frac{\omega_p^2\tau^2}{1+\omega^2\tau^2}, \tag{3.9}$$

$$\varepsilon''(\omega)=\frac{\omega_p^2\tau}{\omega(1+\omega^2\tau^2)}. \tag{3.10}$$

Assuming weak damping ($\omega \gg \gamma$), the expression of $\varepsilon(\omega)$can be simplified to:

$$\varepsilon(\omega)=1-\left(\frac{\omega_p}{\omega}\right)^2. \tag{3.11}$$

With this form, the dielectric function is dominated by the real value implying that the absorption is neglected. It can be seen that for frequencies below the plasma frequency

($\omega \ll \omega_p$), the dielectric permittivity is negative and metal behaves like light reflecting material. For high frequencies ($\omega \gg \omega_p$), the metal behaves as dielectric material and light can be transmitted as if the metal is a transparent material. Complex refractive index n of metal can be obtained from the definition of complex refractive index and permittivity and can be expressed as, $\varepsilon(\omega) = \varepsilon'(\omega) + \varepsilon''(\omega) = n^2$. For our investigation, the real and imaginary parts of the permittivity of gold, silver and copper is calculated by using Drude model and is given in Fig 3.1. Here ω_p for gold, silver and copper are 1.38×10^{16}, 1.39×10^{16}, 1.34×10^{16}, respectively; Again τ for gold, silver and copper are 9.3×10^{-15}, 3.1×10^{-14}, 6.9×10^{-15}, respectively.

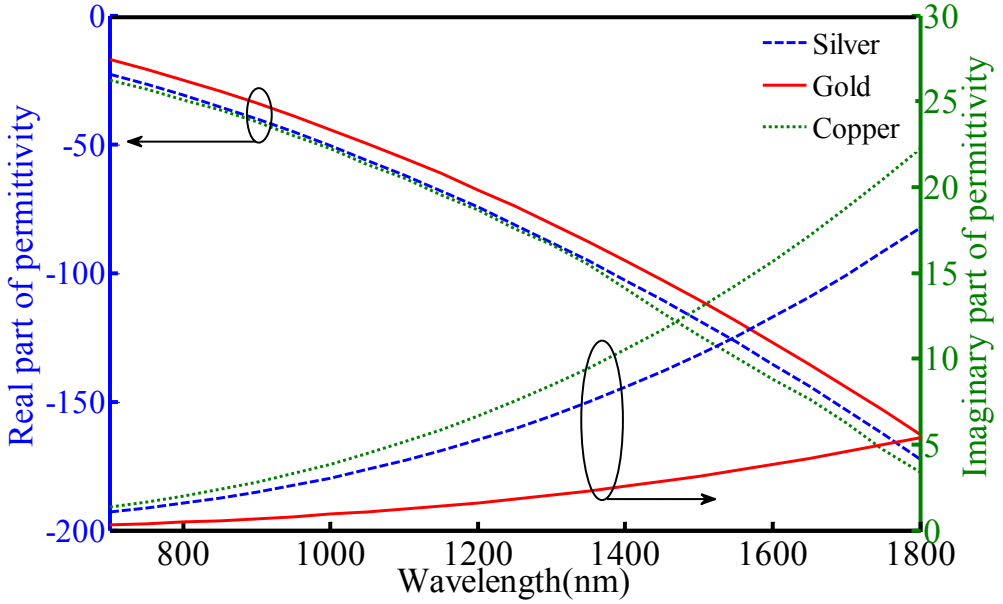

Fig. 3.1 Real and imaginary parts of the permittivity of gold, silver and copper calculated from drude model.

3.2 Maxwell's equations and wave equation

The Maxwell's equations which provide the basic equations governing the electromagnetic response

$$\nabla \times \vec{E} = -\frac{\partial \vec{B}}{\partial t} \quad \text{(Faraday's Law)}, \tag{3.12}$$

$$\nabla \times \vec{H} = \frac{\partial \vec{D}}{\partial t} + \vec{J} \quad \text{(Ampere's Law)}, \tag{3.13}$$

$$\nabla . \vec{D} = \rho_v \quad \text{(Gauss's Law)}, \tag{3.14}$$

$$\nabla . \vec{B} = 0 \quad \text{(Gauss's Law for Magnetic Fields)}, \tag{3.15}$$

where $\vec{E}$ is the electric field (V/m), $\vec{H}$ is the magnetic field (A/m), $\vec{D}$ is the dielectric flux (C/m), $\vec{B}$ is the magnetic flux density (T), $\vec{J} = \sigma\vec{E}$ is the conduction current density of free charges, and ρ_v is the free charge density. The fields are related by material properties

$$\vec{D} = \varepsilon_0\vec{E} + \vec{P}, \tag{3.16}$$

$$\vec{B} = \mu_0\vec{H} + \vec{M}, \tag{3.17}$$

where $\varepsilon_0$is the free-space dielectric permittivity, which is equal to 8.85×10^{-12} (F/m), μ_0 is the free-space magnetic permeability, which is equal to $4\pi \times 10^{-7}$ (H/m), $\vec{P}$ is the polarization density field for the medium, which is interpreted as the dipole moment per unit volume and $\vec{M}$ is the magnetization, which is the magnetic moment per unit volume. In a non-magnetic medium such as dielectric medium, the magnetization term vanishes ($\vec{M}$=0). In addition, we primarily consider in a dielectric medium that contains no free charge (ρ_v = 0) and no free currents ($\vec{J}$ = 0). Taking curl on Eqn. (3.12) and using Eqn. (3.13) we get

$$\nabla \times \nabla \times \vec{E} = -\mu_0 \frac{\partial^2 \vec{D}}{\partial t^2}\,. \tag{3.18}$$

Now using the vector identity for left hand side and using Eqn. (3.14) for isotropic source-free (ρ_v = 0) media, one can obtain the wave equation as

$$\nabla^2\vec{E} - \frac{\varepsilon}{c^2}\frac{\partial^2\vec{E}}{\partial t^2} = 0, \tag{3.19}$$

where ε is the frequency dependent permittivity of material and is written for $\varepsilon(\omega)$. Here $c = 1/\sqrt{\varepsilon_0\mu_0}$ is the velocity of light in free space. Assuming a harmonic time dependence $\vec{E}(\vec{r},t) = \vec{E}(\vec{r})e^{-i\omega t}$, the above equation can be deduced as the following Helmholtz equation

$$\nabla^2\vec{E} + k_0^2\varepsilon\vec{E} = 0, \tag{3.20}$$

where $k_0 = \frac{\omega}{c}$ is the free space wave number.

3.3. Properties of SPPs on planar surfaces

3.3.1. Dispersion relation of surface plasmons on a smooth metal surface

SPPs, excited from coupling of an electromagnetic field to the free electron in a metal, are electromagnetic surface waves propagating along a metal-dielectric interface. To understand the optical behavior of SPPs, we consider a simple planer metal-dielectric structure, as shown in Fig. 3.2, where a dielectric material ($x > 0$), is located on top of a

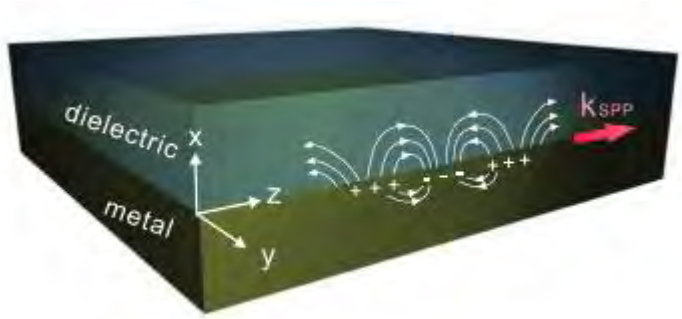

Fig. 3.2 SPP propagating at the interface between metal and dielectric when excited by the TM wave [42].

metal ($x < 0$). The dielectric medium has a frequency dependent positive real dielectric constant ε_d and is assumed to be isotropic and non-absorbing. The metal is isotropic and has a frequency dependent complex dielectric function given by $\varepsilon_m(\omega) = \varepsilon'_m(\omega) + i\varepsilon''_m(\omega)$.

Consider the SPP propagating in the z direction and the transverse-magnetic (TM) wave with magnetic field out of the plane. The electric and magnetic fields in the dielectric medium ($x > 0$) can be written as

$$\overrightarrow{E_d} = (E_{xd},\ 0,\ E_{zd})e^{i(k_{xd}x + k_{zd}z - \omega t)}, \tag{3.21}$$

$$\overrightarrow{H_d} = (0, H_{yd}, 0)e^{i(k_{xd}x + k_{zd}z - \omega t)}, \tag{3.22}$$

In the metal ($x < 0$), the electric and magnetic fields are given by

$$\overrightarrow{E_m} = (E_{xm},\ 0,\ E_{zm})e^{i(-k_{xm}x + k_{zm}z - \omega t)}, \tag{3.23}$$

$$\overrightarrow{H_m} = (0, H_{ym}, 0)e^{i(-k_{xm}x + k_{zm}z - \omega t)}. \tag{3.24}$$

From Maxwell's Eqns. (3.12)–(3.15), we have

$$\nabla \times \overrightarrow{H_i} = \varepsilon_i \frac{\partial \overrightarrow{E_i}}{\partial t}, \tag{3.25}$$

where the subscript i denotes the materials and and ε is the dielectric permittivity in the respective material. It can be expanded as

$$L.H.S. = \left(\frac{\partial H_{zi}}{\partial y} - \frac{\partial H_{yi}}{\partial z}\right)\hat{x} + \left(\frac{\partial H_{xi}}{\partial z} - \frac{\partial H_{zi}}{\partial x}\right)\hat{y} + \left(\frac{\partial H_{yi}}{\partial x} - \frac{\partial H_{xi}}{\partial y}\right)\hat{z}$$

$$= ik_{zi}H_{yi}e^{i(k_{xi}x + k_{zi}z - \omega t)}\hat{x} + ik_{xi}H_{yi}e^{i(k_{xi}x + k_{zi}z - \omega t)}\hat{z}, \tag{3.26}$$

$$R.H.S. = (E_{xi}, 0, E_{zi})(-i\omega\varepsilon_i)e^{i(k_{xi}x + k_{zi}z - \omega t)}. \tag{3.27}$$

Using the relation from Eqn. (3.26) and (3.27) and apply them to the metal-dielectric interface (m and d indicate the metal and the dielectric, respectively). We obtain

$$\frac{k_{xm}}{\varepsilon_m}\frac{H_{ym}}{H_{yd}} = -\frac{k_{xd}}{\varepsilon_d}\frac{E_{zm}}{E_{zd}}. \tag{3.28}$$

Applying the boundary condition where the tangential components of the electric field and magnetic field are continuous at the interface, i.e., $E_{zm} = E_{zd}$ and $H_{ym} = H_{yd}$ yields

$$\frac{k_{xm}}{k_{xd}} = -\frac{\varepsilon_m}{\varepsilon_d}. \tag{3.29}$$

The relationship in Eqn. (3.29) indicates that surface plasmons can only be excited when the dielectric constants of the two media of the interface are of opposite signs. This is achieved through the use of metal which has a negative dielectric constant.

The wave numbers are related by

$$k^2 = k_x^2 + k_z^2 = \varepsilon_i \left(\frac{\omega}{c}\right)^2. \tag{3.30}$$

From Eqn. (3.29) and (3.30), we find

$$k_z^2 = \varepsilon_m \left(\frac{\omega}{c}\right)^2 - k_{xm}^2 \qquad \text{(metal, } x < 0\text{)}, \tag{3.31}$$

$$k_z^2 = \varepsilon_d \left(\frac{\omega}{c}\right)^2 - \left(-k_{xm}\frac{\varepsilon_d}{\varepsilon_m}\right)^2 \quad \text{(dielectric, } x > 0\text{)}. \tag{3.32}$$

Substituting Eqn. (3.31) into Eqn. (3.32) yields

$$k_z^2 = \left(\frac{\omega}{c}\right)^2 \left(\frac{\varepsilon_d \varepsilon_m}{\varepsilon_d + \varepsilon_m}\right). \tag{3.33}$$

With $\varepsilon_m = \varepsilon_m' + i\varepsilon_m''$ and $\varepsilon_m'' < |\varepsilon_m'|$, the dispersion relation for the SPP at a metal-dielectric interface can be written as

$$\mathrm{Re}(k_z) = \left(\frac{\omega}{c}\right)\sqrt{\frac{\varepsilon_d \varepsilon_m'}{\varepsilon_d + \varepsilon_m'}}, \tag{3.34}$$

$$\mathrm{Im}(k_z) = \left(\frac{\omega}{c}\right)\left(\frac{\varepsilon_d \varepsilon_m'}{\varepsilon_d + \varepsilon_m'}\right)^{\frac{3}{2}} \frac{\varepsilon_m''}{2\varepsilon_m'^2}. \tag{3.35}$$

The above equations show the dispersion characteristics of a planar SPP, where the frequency dependent dielectric function of the dielectric ε_d can be calculated by the Sellmeier expansion [43] and the complex frequency dependent dielectric function of metal ε_m can be obtained from the Drude model as discussed in Section 3.1. From the Drude model, for very small damping factor γ, the value of ε_m reduces to

$$\varepsilon_m = 1 - \frac{\omega_p^2}{\omega^2}. \tag{3.36}$$

By substituting the value of ε_m from above equation in Eqn. (3.33) and considering $k_z \to \infty$, we can derive an expression for the surface plasmon frequency as

$$\omega_{sp} = \frac{\omega_p}{\sqrt{1+\varepsilon_d}}. \tag{3.37}$$

3.3.2 Propagation length and skin-depth of surface plasmons on a smooth surface

The length over which the intensity of the surface plasmon wave decreases to 1/*e* of its maximum value is called the propagation length. The intensity of the SPP decays while travelling in the *z*-direction according to $e^{-2\mathrm{Im}(k_z)z}$ [4]. Thus, the SPP propagation length is given by

$$L_{sp} = \frac{1}{2\mathrm{Im}\,(k_z)} = \left(\frac{c}{\omega}\right)\left(\frac{\varepsilon_d \varepsilon'_m}{\varepsilon_d+\varepsilon'_m}\right)^{\frac{-3}{2}} \frac{\varepsilon'^2_m}{\varepsilon''_m}. \tag{3.38}$$

The electric field decay of SPP field along the transverse direction (*x*-direction) can be deduced by the propagation constant in the *z* direction from Eqn. (3.30), (3.31) and (3.32), with the assumption $\varepsilon''_m < \left|\varepsilon'_m\right|$ and $\varepsilon'_m + \varepsilon_d < 0$. The skin depth ($\delta=1/k_{xi}$) (the distance where the field falls to 1/*e* of its original value) of the electric field can be obtained as

$$\delta_{metal} = \left(\frac{c}{\omega}\right)\sqrt{\frac{\varepsilon_d+\varepsilon_m}{\varepsilon_m^2}}, \tag{3.39}$$

$$\delta_{dielectric} = \left(\frac{c}{\omega}\right)\sqrt{\frac{\varepsilon_d+\varepsilon_m}{\varepsilon_d^2}}. \tag{3.40}$$

3.4 SPPs on metallic wire

SPPs can also be generated in metallic wires. First we have investigated with rectangular wire, which was followed by circular wire. The geometry of interest to the present study is that of a metallic stripe or a wire of rectangular cross section bounded on all sides by a lossless dielectric medium [44]. The geometry we have studied is shown in Fig. 3.3. A metal stripe of thickness t = 0.1 μm and width w = 1 μm is considered which is surrounded on all sides by a lossless dielectric medium. The total investigation is done for the wavelength λ = 1.55 μm. The metal used is silver with a dielectric constant ε_m = − 125.735 + i3.233 as obtained from experimental values of Johnson and Christy [45]. The dielectric constant of the lossless medium was 12.25. When the metal is in the form of a film, SPP occur on each side of the film as shown in Fig. 3.4. For a film with sufficiently small thickness, surface modes couple to each other, producing supermodes. In the case of a metal film bounded on both sides by the same dielectric, the supermodes, as represented by the magnetic field component tangential to the interface, have either symmetric or asymmetric profiles with the plane of symmetry being midway between the interfaces. The generation of SPPs on solid metallic wire surface enables the realization of plasmonic waveguide when the loss incurred by SPPs can be minimized.

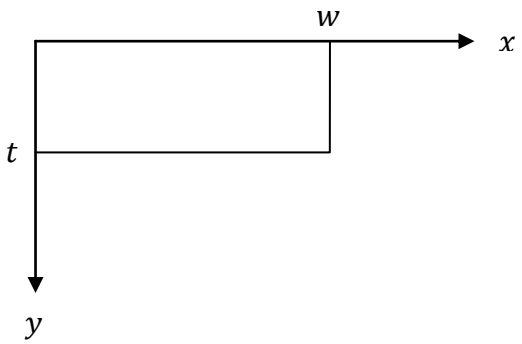

Fig. 3.3 Schematic dimension of the investigated metallic slab wire.

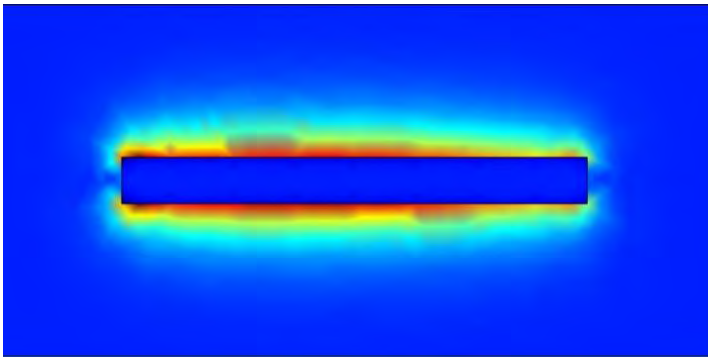

Fig. 3.4 A closer look of the excitation of SPPs on both side of the metal stripe wire, bounded on all sides by lossless dielectric medium.

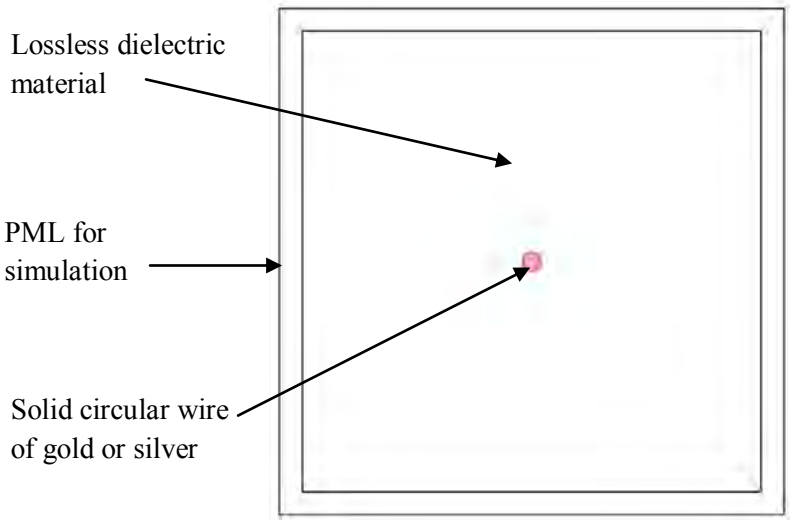

Fig. 3.5 Schematic of the simulation setup used for generating SPPs on circular metallic wire.

Both gold and silver wires are considered for investigation with circular wire. Gold and silver wires are taken with a diameter of 0.4 μm, which is bounded on all sides by a lossless dielectric material as shown in Fig. 3.5. The total investigation is done for the wavelength of λ =1.55 μm. The wavelength dependent dielectric constant for gold and silver is calculated from Drude model. The dielectric constant of lossless media

surrounding the metal wire has a value of 12.25. When the circular metal wire has sufficiently small radius it can effectively generate the surface modes surrounding the total circular wire. A closer look of the generated surface mode surrounding the metal wire (gold or silver) is shown in Fig. 3.6.

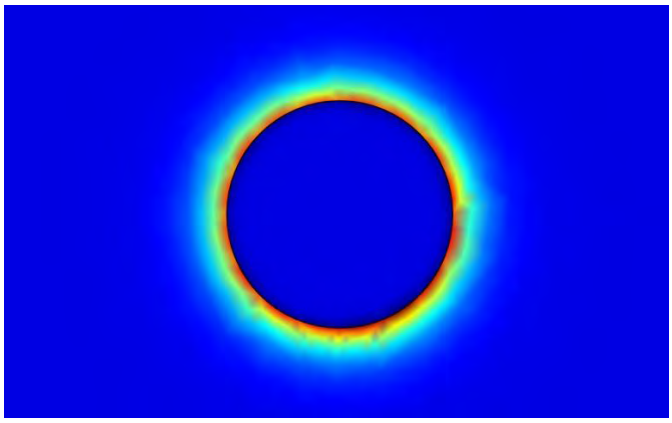

Fig. 3.6 A closer look of the excitation of SPPs on the surface of a circular metal (gold or silver) wire bounded by lossless dielectric medium.

3.5 How sensing can be accomplished

The resonance phase matching happens between an incident electromagnetic wave and high loss plasmonic wave at the metal-analyte interface at a specific combination of the angle of incidence and wavelength. Mathematically, phase matching constitutes equating the effective refractive index of the two modes at a given wavelength of operation or specific angle of incidence.

The excitation of surface plasmons at metal-dielectric interface results in the transfer of energy from incident photons to surface plasmons, which reduces the energy of the reflected light. If the normalized reflected intensity (R), which is basically the output signal, is measured as a function of incident angle (θ) by keeping other parameters and components (such as frequency, metal layer, and dielectric layer) unchanged, then a sharp dip is observed at resonance angle due to an efficient transfer of energy to surface plasmons as given in Fig. 3.7.

For a given frequency of the light source and the dielectric constant of metal film one can determine the dielectric constant (ε_s) of the sensing layer adjacent to metal layer using Eqn. (1.4) if the value of the resonance angle (θ_{res}) is known. The resonance angle is experimentally determined by using angular interrogation method. Resonance angle is very sensitive to variation in the refractive index of the sensing layer. Increase in refractive index of the sensing layer increases the resonance angler. For wavelength interrogation method, for a fixed angle of incidence of the light source and the dielectric constant of metal film one can determine the dielectric constant (ε_s) of the sensing layer adjacent to the metal layer using Eqn. (1.5). Here (θ_{res}) is being replaced by (λ_{res}) which can be determined experimentally by analyzing the output spectrum of light.

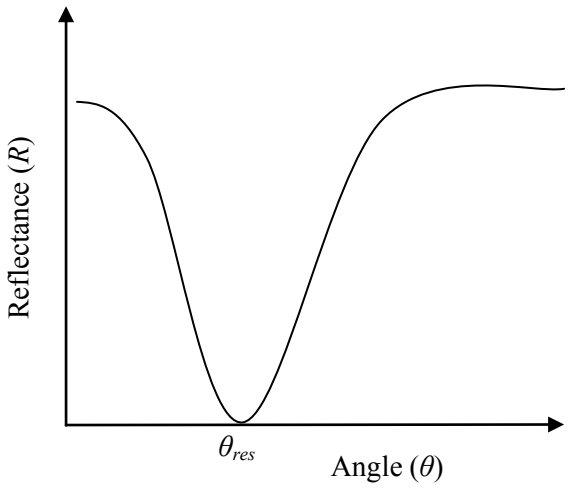

Fig. 3.7 Reflectance (R) as a function of incidence angle (θ) at the prism-metal interface (angular interrogation). A sharp drop in reflected signal is observed at angle θ_{res}.

Again, surface plasmons, which propagate in the metal-dielectric interface, are extremely sensitive to the variations of refractive index of the dielectric. As the real part of the plasmon refractive index depends strongly on the value of the analyte refractive index, the resonance condition of phase matching between the waveguide core mode and plasmonic mode will also be sensitive to the changes of analyte refractive index. So with the change of the analyte refractive index, the resonance wavelength will also shift. When a new dielectric material with a different refractive index will be present in the analyte channel, it will shift the resonance wavelength. From the amount of shift in the position of the resonance wavelength, one can, in principle, extract the value of changes in the analyte refractive index. This transduction mechanism is commonly used for the detection of the analyte bulk refractive index changes. By implementing and optimizing the design criteria, if we can achieve greater shift of the resonance wavelength for very small change in the analyte refractive index, we can achieve higher sensitivity. For effective and accurate detection, achieving higher sensitivity is of utmost importance.

3.6 Performance parameters of SPR sensors

3.6.1 Sensitivity

For angular interrogation method sensitivity of a SPR sensor depends on how much the resonance angle shifts with a change in refractive index of the sensing layer. For very small change in the analyte index, if the shift of resonance angle is large, the sensitivity is large. Fig. 3.8 shows a plot of reflectance as a function of angle of the incident light beam for sensing layers with refractive indices n_s and $n_s+\delta n_s$. Increase in refractive index by δn_s shifts the resonance curve by $\delta\theta_{res}$ angle. The sensitivity of a SPR sensor with angular interrogation is defined as [46]

$$S_n = \frac{\delta\theta_{res}}{\delta n_s}. \tag{3.41}$$

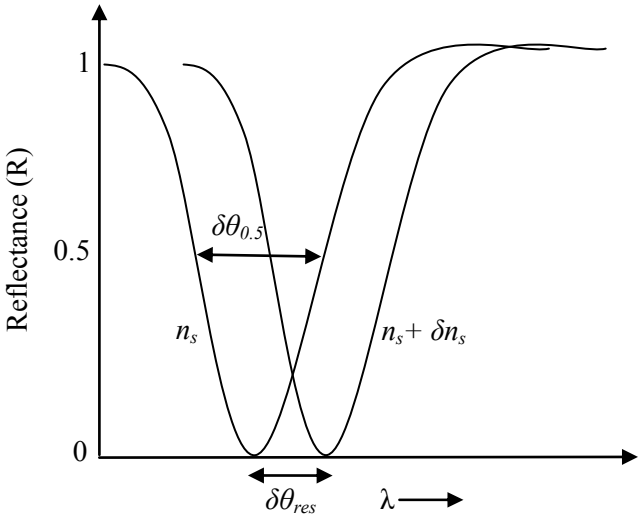

Fig. 3.8 The shift in resonance angle ($\delta\theta_{res}$) with a change in refractive index of the sensing layer (n_s) by δn_s. $\delta\theta_{0.5}$ is the width of the curve at half reflectance for sensing layer refractive index n_s.

In the SPR sensor based on wavelength interrogation, the incident angle is fixed and the resonance wavelength λ_{res} is determined corresponding to the refractive index of the sensing layer n_s. If the refractive index of the sensing layer is altered by δn_s the resonance wavelength shifts by $\delta\lambda_{res}$. The sensitivity (S_n) of an SPR sensor with spectral interrogation method is defined as [46]

$$S_n = \frac{\delta\lambda_{res}}{\delta n_s}. \tag{3.42}$$

The spectrum of the output in the wavelength interrogation method is shown in Fig. 3.9.

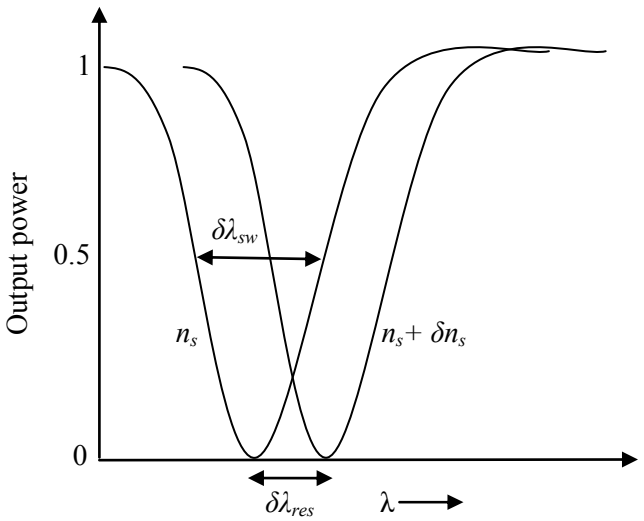

Fig. 3.9 The shift in resonance wavelength ($\delta\lambda_{res}$) with a change in refractive index of the sensing layer (n_s) by δn_s. $\delta\lambda_{sw}$ is the spectral width of the curve at FWHM output power point corresponding to sensing layer refractive index n_s.

3.6.2 Detection accuracy or SNR

The detection accuracy or the SNR of a SPR sensor depends on how accurately and precisely the sensor can detect the resonance angle and hence, the refractive index of the sensing layer. Apart from the limitations of a real instrument, the accuracy of detection of resonance angle further depends on the width of the SPR curve. Narrower the SPR curve, higher is the detection accuracy. Therefore, if $\delta\theta_{0.5}$ is the angular width of the SPR response curve corresponding to 50% reflectance, the detection accuracy of the sensor can be assumed to be inversely proportional to $\delta\theta_{0.5}$ as shown in Fig. 3.8. The SNR of the SPR sensor with angular interrogation is, thus, defined as [47]

$$SNR = \frac{\delta\theta_{res}}{\delta\theta_{0.5}}. \tag{3.43}$$

Actual SNR of the real SPR sensing system critically depends on how well one measures the signals with real instruments.

In wavelength interrogation method also the accuracy of the detection of the SPR wavelength (λ_{res}) depends on the width of the response curve as shown in Fig. 3.9. The spectral width of the SPR curve should be small for an accurate measurement of the resonance wavelength. Therefore, similar to angular interrogation, if $d\lambda_{sw}$ is the spectral width of the response curve at some reference output power value, the SNR of the SPR sensor utilizing spectral interrogation can, therefore, be written as [47]

$$SNR = \frac{\delta\lambda_{res}}{\delta\lambda_{sw}}. \tag{3.44}$$

3.6.3 Sensing range

As far as the operating range is considered, it is the range of sensing layer refractive indices n_s that a sensor can detect for a given wavelength range. For instance, if one wants to operate the sensor in the visible region only, then the range of n_s values with their corresponding λ_{res} falling in the visible region will decide the operating range of the sensor. No established empirical formula for determining the sensing range is being used, rather, one needs to find it through the sensing capability of the respective sensor for particular type of analyte.

3.6.4 Detection linearity

Detection linearity is the response with which the resonance wavelength shifts for corresponding change in the analyte index. We need to evaluate this value to underatnd the capability of a particular type of sensor to be used as calibration sensor. If the shift of resonance wavelngth for corresponding change in analyte index is highly linear, then the particular sensor can be used as calibration sensor. From the vlaue of calibration relations of a sensor, one can bring out the value of the particular analyte index. If we have the resonance wavlength from optical spectrum analyser, which is evident by a sharp dip, we can plot the resonace wavelength in the calibration relations and can find

out the refractive index of that analyte. As an example the calibration relation of our proposed sensor is given in Fig. 3.10. From Fig. 3.10 it is evident that if we know the resonance wavelength for any analyte, we can find out the refractive index of that particular analyte from the graph. But, very high detection linearity of particular sensor is required to obtain the analyte refractive index in this method.

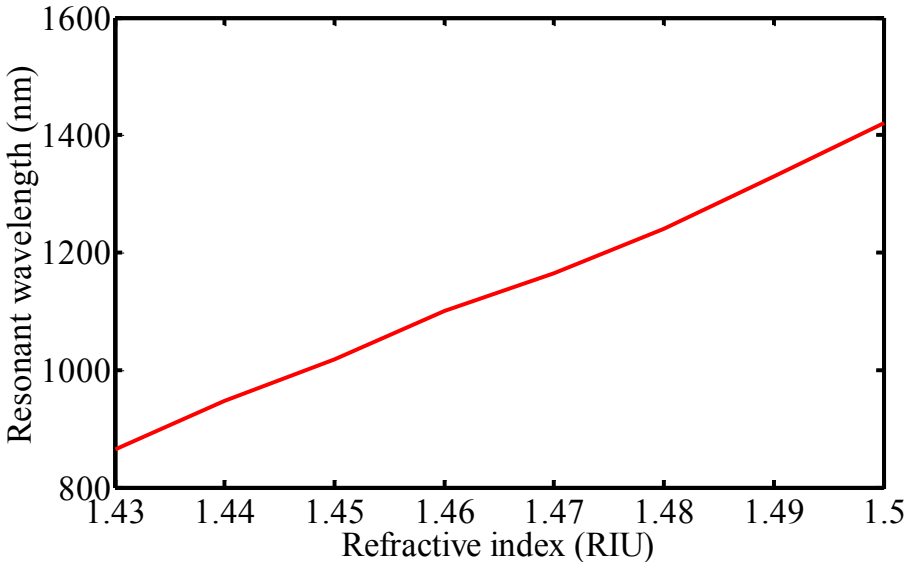

Fig. 3.10 Detection linearity in terms of shift of resonance wavlength for change in analyte index.

CHAPTER 4

DESIGN AND PERFORMANCE ANALYSIS OF PCF BASED SPR SENSOR

PCF based SPR sensors are designed conventionally with hexagonal lattice structure as discussed in chapter 2. Being simpler in geometry than hexagonal lattice, square lattice structure can be a candidate for use in SPR based sensor, which is proposed here. Again, to enhance the fluid flow in the sensor, multiple analyte channels have been proposed in PCF based SPR sensor [8], [36]. But, the use of multiple analyte channels in SPR sensor probe entails few disadvantages such as more gold consumption in analyte channel coating and need of more analyte sample than single analyte channel based SPR sensor. Co-channel interference from neighboring analyte channels is also an issue in multiple analyte channel based SPR sensor. SPR sensor with single analyte channel will be free from all these disadvantages and is investigated and proposed here.

Usually, the metallic layer used in SPR sensor consists of either gold or silver. Gold demonstrates a higher shift of resonance parameter to change in refractive index of sensing layer and is chemically stable. Silver, on the other hand, displays a narrower resonance curve causing a higher detection accuracy or SNR, but has a poor chemical stability. The oxidation of silver happens as soon as it is exposed to air and especially to water, which makes it difficult to use to get a reliable sensor for practical applications. Treatment of the silver surface by a thin and dense cover is therefore required. As the use of gold shows higher shifts in resonance parameters which consequently helps in achieving higher sensitivity, silver can be coated with gold to achieve both higher sensitivity and detection accuracy. So, the need for an optimum combination of metals in the analyte channel coating is imperative which is also being investigated here.

Besides gold, other metals can also be used for analyte channel coating. The capability of other metals such as the use of silver (Ag) or copper (Cu) in analyte channel coating for SPR sensor applications has also been analyzed. The copper also has some limitations like silver. It is chemically vulnerable against oxidation and corrosion, therefore, its protection is required for a stable sensing application. Also it may be noted from Eqn. (1.4) that the SPR condition depends upon the refractive index of the material of the fiber core. Therefore, if a PCF is fabricated by adding dopants in the fiber core, the sensitivity of the sensor can be enhanced or tuned. Basing on this assumption, sensor performance is evaluated by adding three dopants (13.5% GeO_2, 9.1% P_2O_5, 5.2% B_2O_3) separately with pure silica.

Different performance parameters namely sensitivity, detection accuracy or SNR, sensing range and detection linearity of the proposed sensor are being evaluated to find the suitability of all the proposed design considerations. To formulate all the

above mentioned design and analysis, numerical modeling technique is used, which plays an important role in designing and characterizing the PCF based sensors. While designing fiber waveguide, sensor etc., even the simplest shape in fiber cross section is difficult and cumbersome to deal with analytically. So, to emphasize more on design and evaluation rather than analytical calculation, numerical modeling technique is used. In order to fully appreciate the physics of plasmonics and how they could be embedded in PCF based sensor to get the best sensitivity, a systematic study is carried out with the help of finite element method (FEM), included in the RF module of Comsol Multiphysics™ [48].

4.1 Modeling technique

4.1.1 Finite element method

The finite element method (FEM) or finite element analysis (FEA) is fundamentally a method for obtaining a numeric approximation to a governing differential equation, subject to prescribed boundary conditions, over some geometric domain. The domain is divided into a finite number of smaller non-overlapping regions referred to as elements. All of the elements taken together completely cover the domain of interest like the pieces of a puzzle. Each element contains some number of points referred to as nodes. For example, a 2D problem may use triangular elements, and each element will have at least three nodes, corresponding to the vertex points of the triangle. The elements and nodes together are referred to as the mesh. The dependent variable is approximated over each element by some interpolating function, generally a polynomial. Using this concept, while modeling, we have divided the whole domain of the PCF cross section into small elements using appropriate mesh and obtained the solution for whole domain.

4.1.2 Formulation using FEM

The refractive index of the PCF core is taken as n_1. The cladding consists of a number of air holes with a background of core material. The effective index of the cladding, taken as n_2, is determined as the fundamental space filling mode which is lower than n_1 ensuring that there is at least one confined mode for a single mode PCF and more than one mode for a multimode PCF. For a confined mode, there is no energy flow in the radial direction, thus the wave must be evanescent in the radial direction in the cladding. This is true only if the effective index of the confined mode, n_{eff} is greater than n_2. On the other hand, the wave cannot be radially evanescent in the core region. Thus, $n_1 > n_{\text{eff}} > n_2$. The refractive indices change with the change in wavelength. These different values of indices at different wavelengths are obtained from the corresponding Sellmeier equation. The optical mode analysis is made on a cross-section in the x-y plane of the fiber. The wave propagates in the z-direction and has the form

$$\vec{H}(x,y,z,t) = \vec{H}(x,y)e^{j(\omega t-\beta z)}, \tag{4.1}$$

where ω is the angular frequency and β is the propagation constant. An eigenvalue equation for the magnetic field, $\vec{H}$ is derived from Helmholtz equation

$$\nabla \times \left(n^{-2}\nabla \times \vec{H}\right) - k_0^2 \vec{H} = 0, \tag{4.2}$$

which is solved for the eigenvalue $\lambda = -j\beta$. As boundary condition, along the outside of the cladding, the magnetic field is set to zero. As the amplitude of the field decays rapidly as a function of the radius of the cladding this is a valid boundary condition.

4.1.3 Meshing of the domain

The finite element method approximates a variational problem as a solvable numerical problem by reducing the degrees of freedom of the system to a finite number. The terms discretization and meshing are used within FEA literature to describe this step. In practice, a distribution of discrete points is placed inside and along the boundary of the function. These points, known as vertices or nodes, are where the function will be evaluated. The vertices are then connected to form small, simple and uniform geometries called finite elements. The domain of the discretized unknown function is a composite of these tiny geometries. To illustrate graphically, a cross section of the mesh used for our FEM solution is shown in Fig. 4.1.

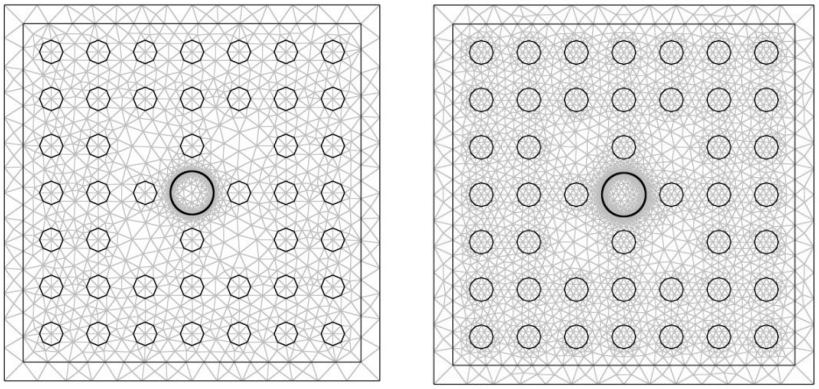

(a) (b)

Fig. 4.1 A cross section of the mesh grid used in our FEM calculation. (a) An unrefined grid and (b) Shows the same grid after adaptive refinement steps.

4.1.4 Boundary and interface conditions

The interior boundaries of the cross-sectional geometry of the PCF are set at continuity boundary conditions. The outermost boundary of the cross-section is set at perfect electric conductor boundary condition when solving for magnetic field intensity, $\vec{H}$. Perfect magnetic conductor boundary condition is used when solving for electric field, $\vec{E}$. This is a valid boundary condition as the radius of the geometry is chosen large enough for the electric or magnetic field to decay to zero.

The perfect magnetic conductor boundary condition,

$$\vec{n} \times \vec{H}=0, \tag{4.3}$$

sets the tangential component of the magnetic field to zero at the boundary. Also, it implies that, $\vec{n} \cdot \vec{D} = 0$ for a perfect magnetic conductor.

The perfect electric conductor boundary condition,

$$\vec{n} \times \vec{E} = 0, \tag{4.4}$$

sets the tangential component of the electric field to zero at the boundary. Also, it implies that, $\vec{n} \cdot \vec{B} = 0$ for a perfect electric conductor.

The continuity boundary condition is the natural boundary condition ensuring continuity of the tangential components of the electric and magnetic fields, given as

$$\vec{n} \times \left(\overrightarrow{H_1} - \overrightarrow{H_2}\right) = 0, \tag{4.5}$$

$$\vec{n} \times \left(\overrightarrow{E_1} - \overrightarrow{E_2}\right) = 0. \tag{4.6}$$

A perfectly matched layer (PML) is an artificial boundary condition implying perfect absorption of incident field. This boundary condition is required for approximating infinite zone beyond the waveguide outer edge to a finite domain of numerical analysis. The key property of a PML that distinguishes it from an ordinary absorbing material is that waves incident upon the PML from a non-PML medium do not reflect at the interface. This property allows the PML to strongly absorb outgoing waves from the interior of a computational region without reflecting them back into the interior. Schematic cross section of the PML used in our work is shown in Fig. 4.2.

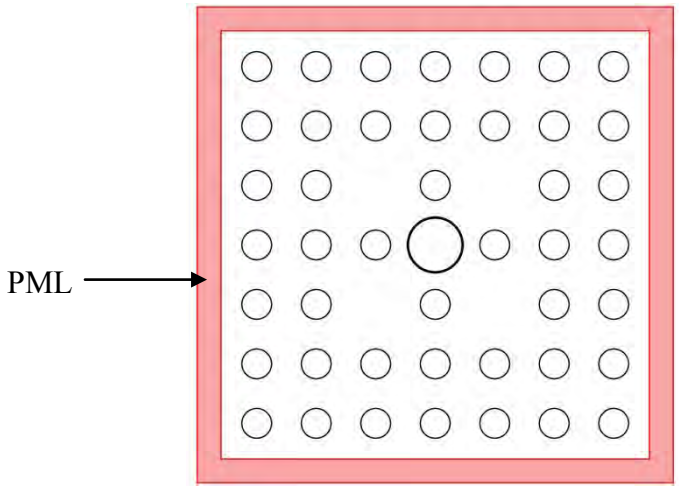

Fig. 4.2 Schematic of PML in the proposed PCF based SPR sensor.
The outer red stripe denotes the PML.

4.2 SPR sensor with hexagonal lattice PCF

To have a comprehensive understanding and in-depth analysis about SPR sensor, the conventionally used H-PCF based SPR sensor has been designed and evaluated first. A schematic cross section of the conventional solid core H-PCF structure is shown in Fig. 4.3 which is modified to be used in SPR sensing system. A schematic cross section of the modified design to be used in SPR sensing, is shown in Fig. 4.4.

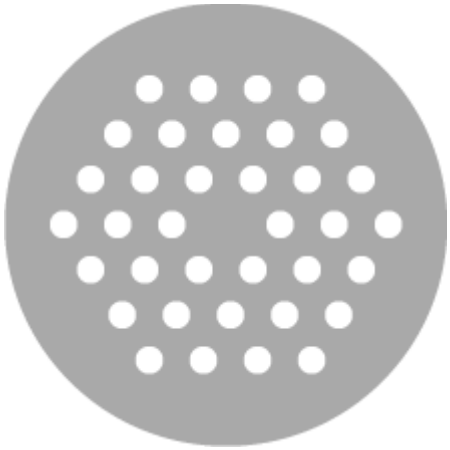

Fig. 4.3 Cross section of a conventional solid core H-PCF. The gray area denotes silica and white circles denote air holes.

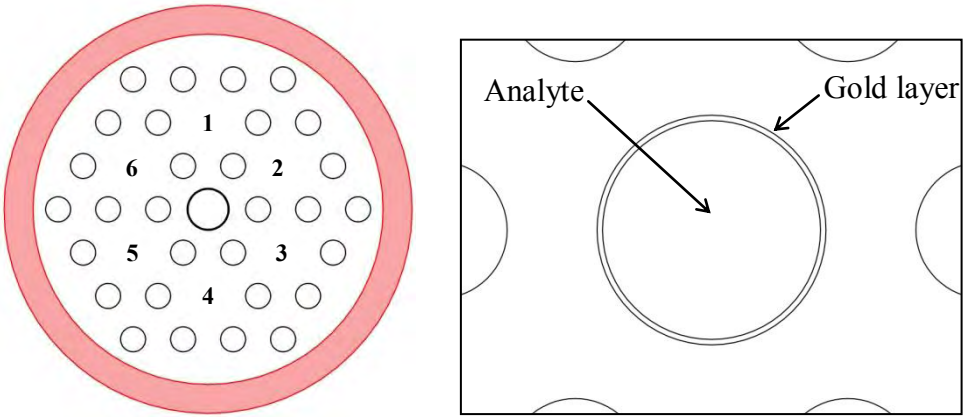

Fig. 4.4 Multi-core hexagonal lattice PCF for SPR sensing application. (a) Schematic cross section, where six cores and PML are marked with arabic numerals and red stripe, respectively. (b) Closer look of the central analyte channel.

Here only one analyte channel is used in the centre of H-PCF. The inclusion of the analyte channel in the centre of the core can effectively increase the overlap between the evanescent field and surface plasmon wave which increases the detection sensitivity of the device. In this design, six cores are formed by eliminating six air holes which are substituted by silica. A hollow central channel is created to allow the

analyte to flow. When light is launched, light will be guided in the cores. The Gaussian-like leaky mode from the core guided light of the six cores generate evanescent field out of TIR, which will excite the plasmonic mode in the metal-analyte boundary. From the evaluation of this design, well defined power concentration in the core guided fundamental mode is obtained as shown in Fig. 4.5 (a), 3D representation of which is shown in Fig. 4.5 (b). Here, total power is concentrated in the core guided fundamental mode. Evenly distributed power flow in the six core is evident in both the surface and 3D plot. Plasmonic mode through the coupling of core guided light and surface plasmons is also obtained as shown in Fig 4.6 (a), 3D representation of which is shown in Fig. 4.6 (b). In case of plasmonic mode total power is shifted from core guided mode to plasmonic mode, as evident in both the surface and 3D plot. Also, the surface plot and its corresponding 3D representation confirm the highest power concentration in metal-analyte boundary in case of plasmonic mode.

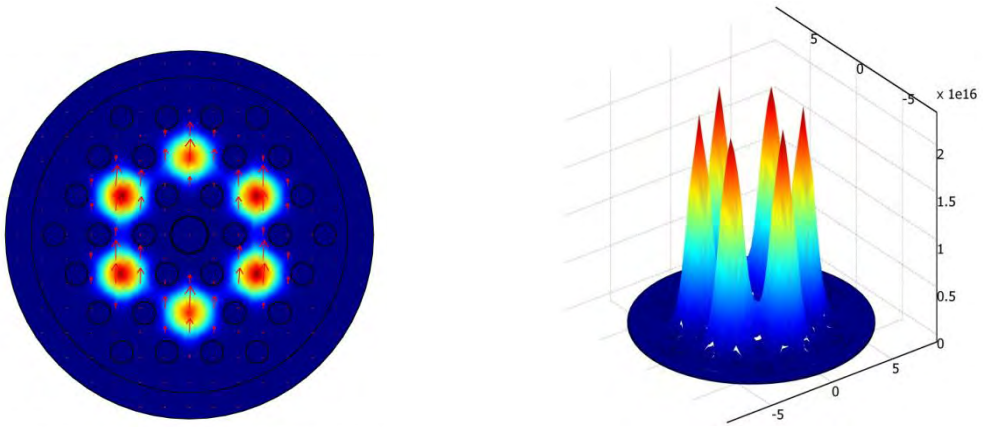

(a) (b)

Fig. 4.5 Fundamental mode of the core guided light in six identical cores of H-PCF based SPR sensor. Power flow is shown in w/m^2.

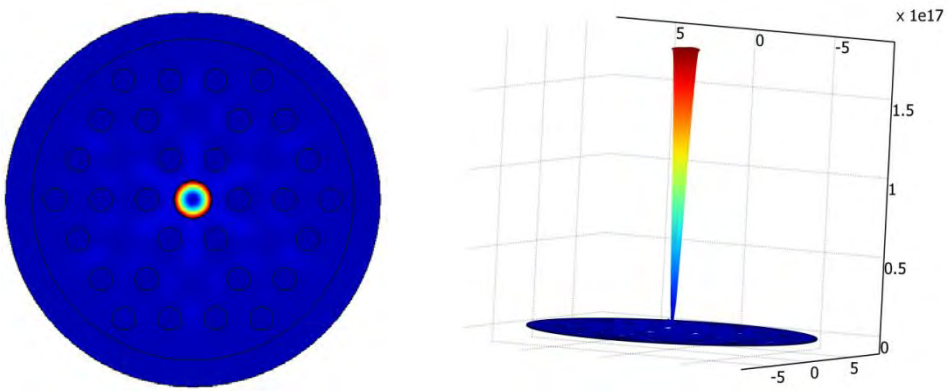

(a) (b)

Fig. 4.6 Excitation of plasmonic mode in the centrally located single analyte channel. Power flow is shown in w/m^2.

Evaluation of the SPR sensor with six identical core H-PCF yields an average sensitivity of 9231 nm/RIU in the sensing range of 1.43-1.53 refractive index. As in this design, the number of analyte channel is reduced to only one, this has effectively minimized the requirement of gold in analyte channel coating. The sensitivity and dynamic sensing range is also high. The change in the resonance wavelength for corresponding change in the analyte refractive index is found to be fairly linear for this design (0.96704). However, this design is also being evaluated by Binbin Shuai et al. [38].

4.3 SPR sensor with square lattice PCF

4.3.1 Design of SL-PCF based SPR sensor

A schematic cross section of the proposed SL-PCF based SPR sensor is shown in Fig. 4.7 (a), while a closer look of the analyte channel and gold layer is shown in Fig. 4.7. (b). Four cores are created by omitting four air holes and substituting those air holes

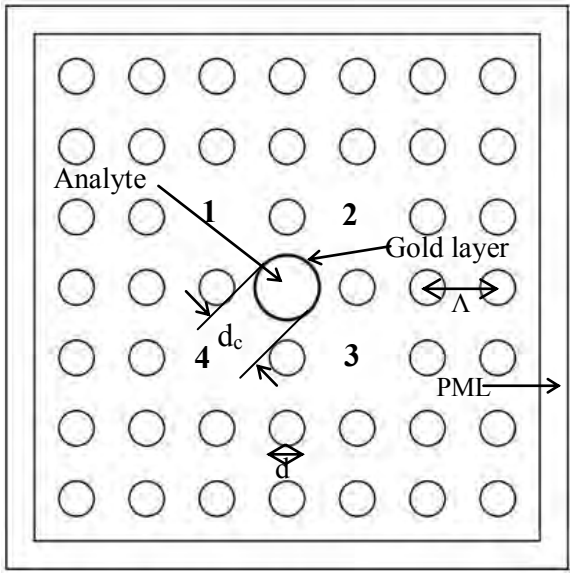

(a)

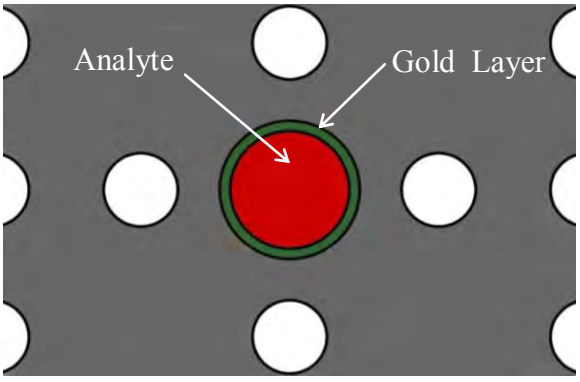

(b)

Fig. 4.7 (a) Schematic cross section of the proposed SPR sensor, (b) Closer look of analyte channel and gold layer.

by silica rods. Cores are marked with arabic numerals 1, 2, 3 and 4. The PCF is made of silica glass with air holes running along the length where the air holes are arranged in square lattice having pitch $\Lambda = 2$ μm. The diameter of the central analyte channel is $d_c = 0.9\Lambda$ and the diameter of the air holes are $d = 0.5\Lambda$. The metalized micro channel is coated with gold of thickness $t = 40$ nm. A perfectly matched layer (PML) is used in the boundary. The dielectric constant of gold is obtained from the Drude model and the wavelength dependent refractive index of silica material is found using Sellmeier equation. The metalized micro channel is filled with aqueous sample named as analyte, with n_a varying from 1.43 to 1.50. For reducing the gold consumption in analyte channel coating and also to reduce co-channel interface, only one analyte channel is used instead of multiple analyte channel. In this design, less sample is needed for detection as the number of analyte channel is only one. Multiple cores are used to increase the coupling between core guided mode and the plasmonic mode.

4.3.2 Results and discussion

The evaluation started for a particular analyte index, say 1.43. Keeping this analyte index fixed, the aim of the simulation and analysis was to find the resonance wavelength through plotting the waveguide core more effective refractive index and plasmonic mode effective refractive index at different wavelength of light. The simulation was conducted by launching light over a range of wavelength starting from 0.70 μm to 1.50 μm with a stepping of 0.5 μm. For a particular wavelength of light, say for 0.70 μm, the complex effective refractive index of waveguide core mode and plasmonic mode is found out through post processing and visually investigating the mode characteristics. Similarly effective refractive index for core guided fundamental mode and plasmonic mode for the whole range of wavelength of light starting from 0.70 μm to 1.50 μm has been obtained. Post processing, after the finite element simulation, has been carried out to find the core guided fundamental mode and the plasmonic mode. As an example, the power concentration of core-guided fundamental mode for $n_a = 1.43$ at λ=1.4 μm is shown in Fig. 4.8 (a), while the 3D representation of the power distribution is shown in Fig. 4.8 (b). Similarly, power concentration of the plasmonic mode for the same analyte index and wavelength of light is given in Fig. 4.9 (a), while the 3D representation is given in Fig. 4.9 (b). Fig. 4.8 (a) exhibits that the total power is concentrated in the core, for core-guided fundamental mode while there is no power in the analyte channel. The 3D representation in Fig. 4.8 (b) also demonstrates the highest power concentration in the centre of the core. Again in Fig. 4.9 (a), the total power is concentrated in the analyte channel for plasmonic mode while there is no power in the core areas. Similar representation in the 3D mode as given in Fig. 4.9 (b) confirms the highest power concentration in the metal-analyte boundary. As we know from the theory of SPR excitation, in case of plasmonic mode, the highest power concentration is available in the metal-dielectric interface which gradually decays from the highest value at the metal-dielectric interface to the lowest value towards the center of the channel. The proposed design resulted highest power

concentration in metal-dielectric interface and the gradual decays of power in the analyte channel centre as shown in the Fig. 4.10. This gradual decrease of power starting from the highest power in metal-analyte interface to the centre of the analyte channel conforms to the theory of plasmonic wave formation as shown in Fig 1.3 in chapter 1. Power flow from the metal-analyte boundary towards the metal width shows that the power of the plasmonic wave decays very rapidly in the metal as shown in the Fig 4.11. This rapid decrease also conforms to the theory of plasmonic wave formation as shown in Fig 1.3 in chapter 1. These power profiles validate the excitation of SPP and the suitability of the proposed design of the SL-PCF for effective utilization in the SPR sensing regime.

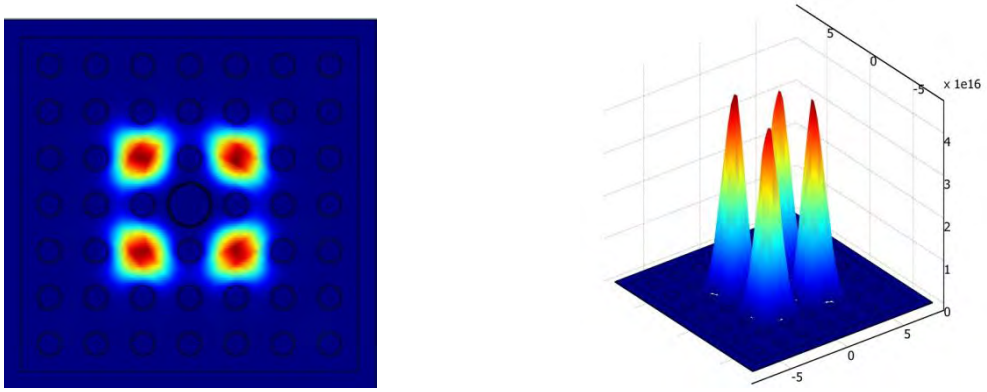

(a) (b)

Fig. 4.8 Concentration of power in core-guided fundamental mode for analyte index n_a = 1.43 and λ=1.40 μm. (a) Surface plot indicates power concentration in the centre of the core, (b) 3D plot also displays and confirms the power concentration obtained in surface plot. Power flow is shown in w/m^2.

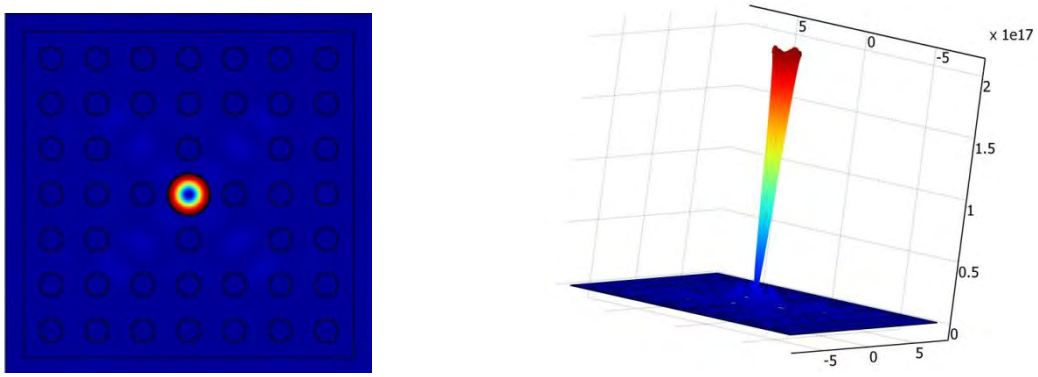

(a) (b)

Fig. 4.9 Concentration of power in the plasmonic mode for analyte index n_a = 1.43 and λ=1.40 μm. (a) Surface plot indicates highest power concentration in the metal-analyte boundary, (b) 3D plot also displays and confirms the highest power concentration obtained in the metal-analyte interface. Power flow is shown in w/m^2.

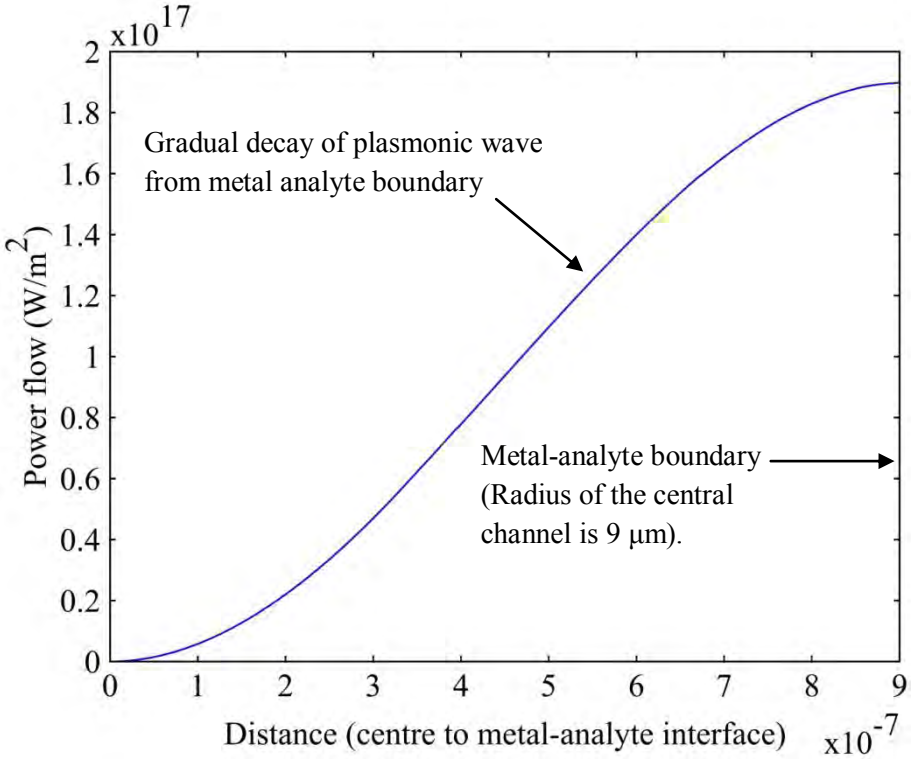

Fig. 4.10 Power flow in the metal-analyte boundary. Highest power is concentrated in the metal-analyte boundary at 0.9 μm distance from the centre of the channel. Distance in x-axis is given in μm.

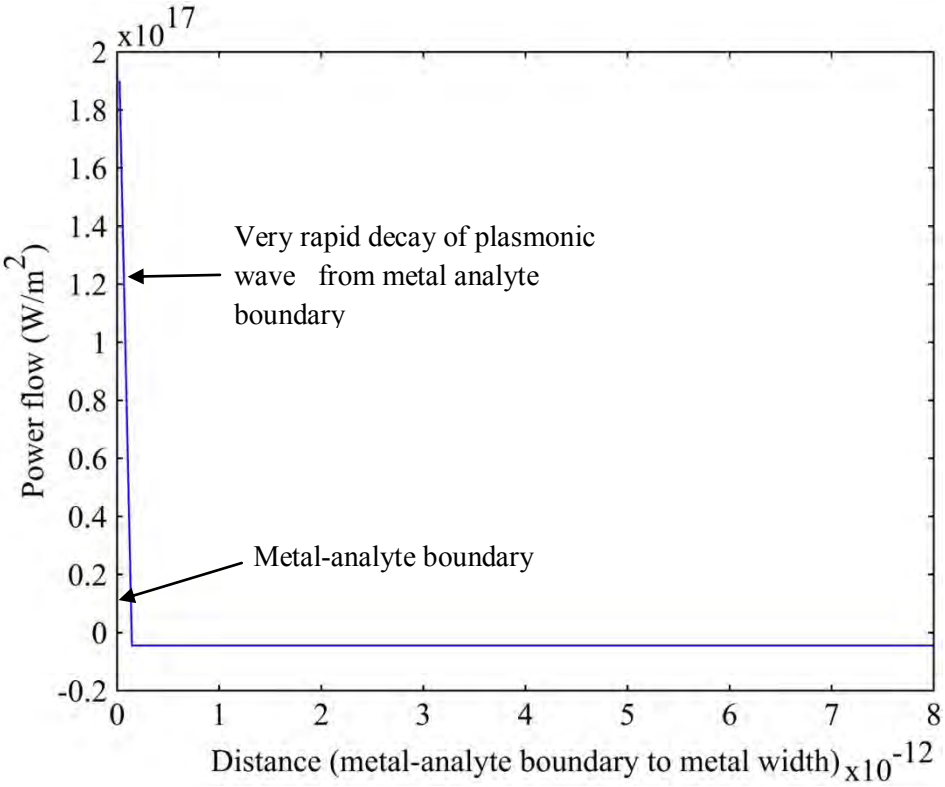

Fig. 4.11 Power flow from the metal analyte boundary (point zero) towards metal width, which exhibits very rapid decay of plasmonic wave in metal. Distance in x-axis is given in μm.

For any particular wavelength, each iteration gives us the value of effective indices for core guided fundamental mode and plasmonic mode. The resonance wavelength is obtained through phase matching by plotting the real part of effective index of waveguide core mode and plasmonic mode. As an example the real part of effective refractive indices of core guided fundamental mode and plasmonic modes when n_a = 1.43, 1.44 and 1.47 are plotted against wavelength ranging from 0.60 μm to 1.40 μm as shown in Fig. 4.12. From Fig. 4.12 it is evident that the real part of effective refractive index of core-guided fundamental mode and plasmonic mode intersect at 865 nm, 948 nm and 1160 nm, respectively and these are the resonance wavelength for three analyte index, i.e. 1.43, 1.44 and 1.47.

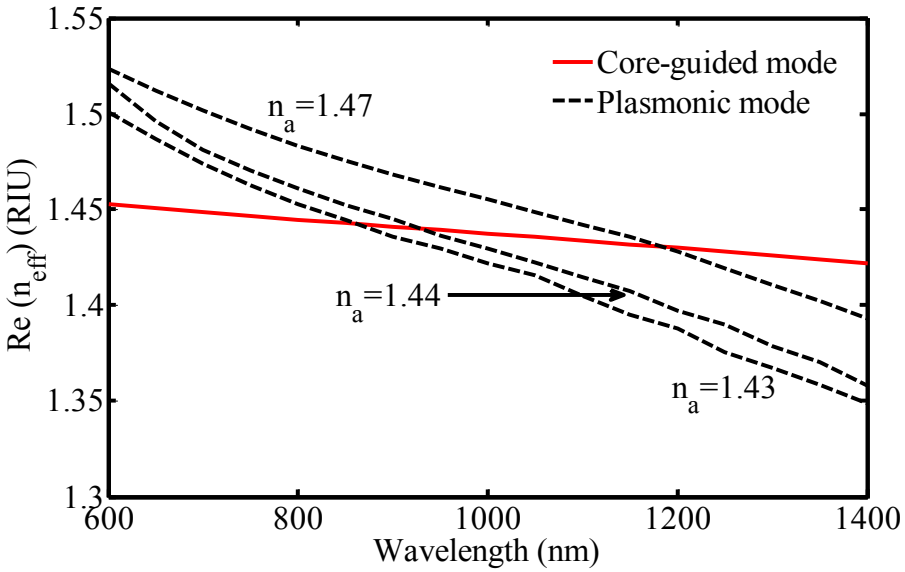

Fig. 4.12 Real part of effective refractive indices of core-guided fundamental mode and plasmonic mode for n_a = 1.43.

We know, at resonance, the core guided light suffer the highest loss as the power is transferred from core guided mode to plasmonic mode for coupling. This loss of solid core PCF is calculated according to the following formula

$$\text{Confinement Loss} = \frac{40\pi}{\ln(10)\lambda}\alpha \quad \text{(dB/m)}, \tag{4.7}$$

where α is the imaginary part of the complex effective index, λ is the wavelength of operation. We have calculated the loss suffered by core guided fundamental mode for all the analyte refractive index in our consideration, i.e. from 1.43 to 1.50. For easy assimilation and clarity, loss characteristics for few analyte refractive indices are given in Fig. 4.13. The corresponding highest loss due to the transfer of energy from fundamental mode to plasmonic mode is evident by loss peak. The resonance wavelength found by phase matching, exactly matches with the loss peak which is

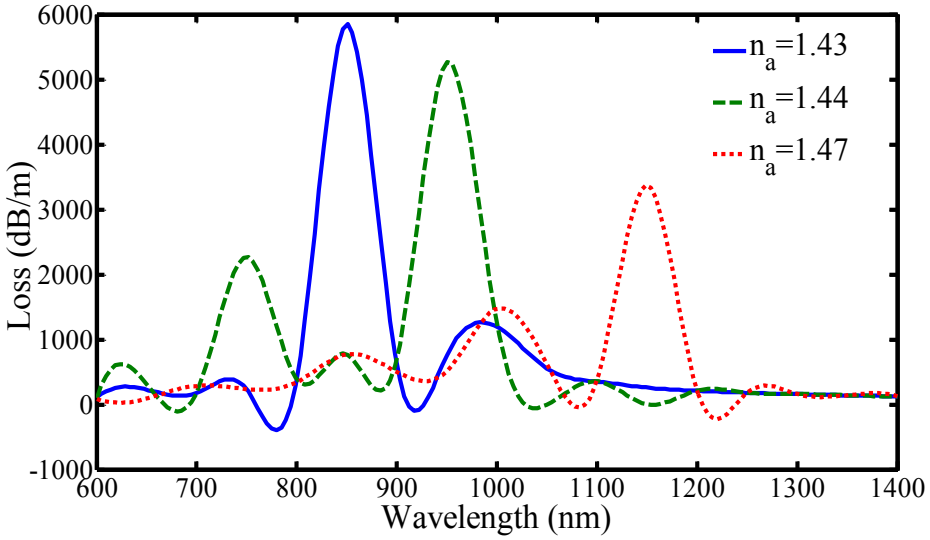

Fig. 4.13 The loss spectra suffered by core guided fundamental mode for different analyte index.

calculated from the imaginary part of the effective indices of the core guided mode following Eqn. (4.7). If we see that the resonance wavelength found in phase matching phenomena coincides with the resonance wavelength found in loss calculation, we can conclude that the excitation of SPR has happened and our proposed design will successfully work as analyte refractive index sensor. To confirm, whether the resonance wavelength found through phase matching and through loss calculation is same, the phase matching phenomenon and loss calculation is plotted together for all analyte index in our consideration, staring from 1.43 to 1.50. For clarity, graph for only two analyte index of 1.44 and 1.47 is shown in Fig. 4.14 (a) and Fig. 4.14 (b). Fig. 4.14 confirms that resonance wavelength found through phase matching and loss calculation coincides. This confirms that the excitation of SPPs happened in our proposed design and there is transfer of power from core guided mode to plasmonic mode at resonance. It is also found that for varying analyte index the resonance wavelength shifts as evident both from dispersion relation and loss peak. With the successful excitation of SPPs and shifts of resonance wavelength, it is also confirmed that the proposed SL-PCF based design can work as SPR sensor.

By calculating the shift of resonance wavelength for corresponding change in the analyte refractive index, the sensitivity of the proposed sensor is calculated. The proposed sensor yields an average sensitivity of 7432 nm/RIU. Another performance parameter, SNR or detection accuracy is calculated from the FWHM power point at resonance wavelength. We know detection accuracy or SNR= $\delta\lambda_{res}/\ \delta\lambda_{0.5}$. So, we need to find out the FWHM point in the normalized transmitted output power as shown in the Fig. 4.15. From Fig. 4.15 the spectral width at the FWHM power point is calculated as 69.0110 nm. The shift of resonance wavelength between 1.43 analyte and 1.44 analyte i.e. $\delta\lambda_{res}$ = 0.948-0.865 = 0.083 μm = 83 nm. So the detection accuracy or SNR = 83 nm/69.0110 nm = 1.202. SNR is a unit less quantity and is inversely proportional to the width of the resonance curve.

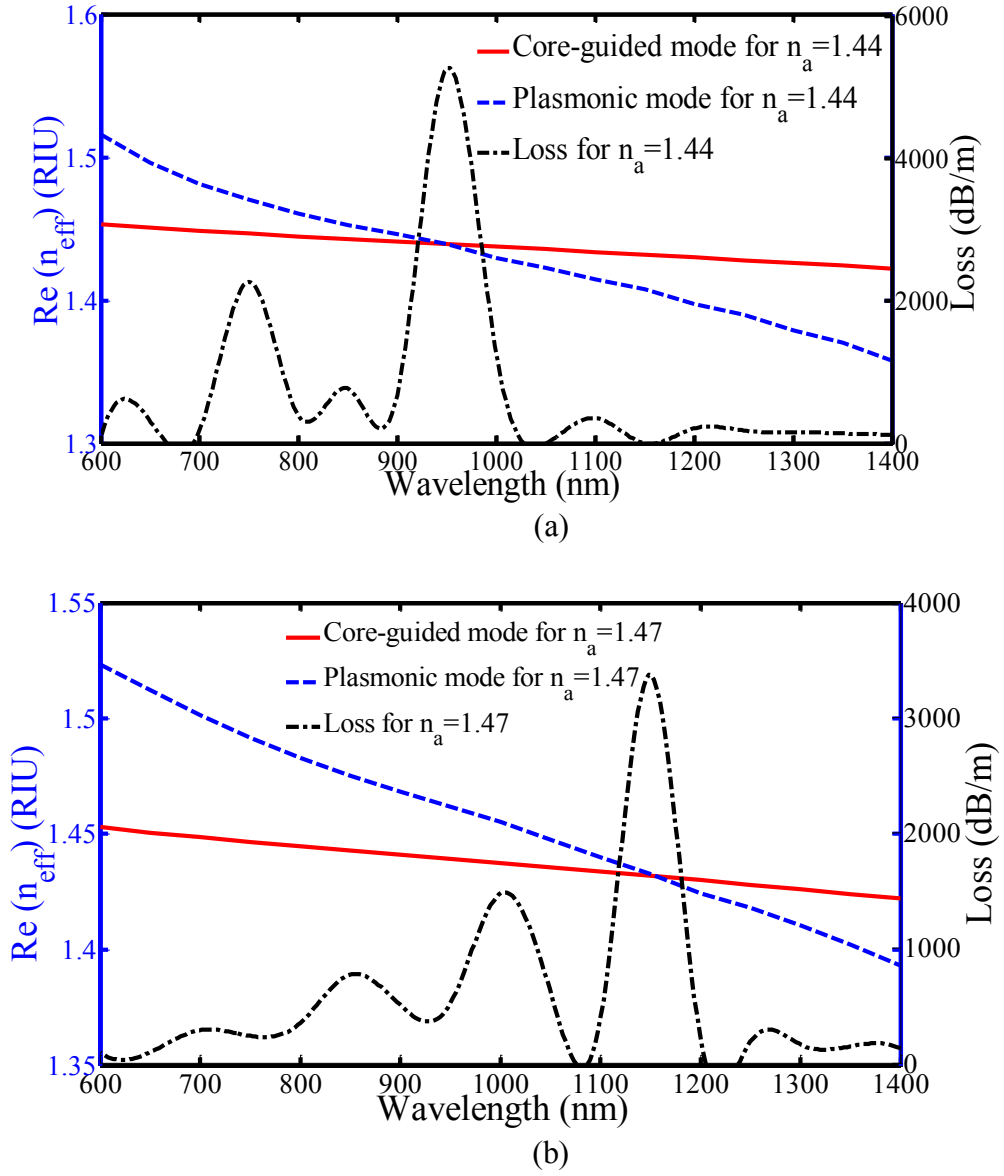

Fig. 4.14 Loss peak and intersection of the effective refractive indices of core-guided fundamental mode and plasmonic mode for (a) n_a = 1.44 and (b) n_a =1.47. For clarity the phenomena are shown in the vicinity of resonance wavelength.

Detection linearity is another important consideration for sensor deign. By plotting the detected analyte refractive index and corresponding shift in the resonance wavelength, we can get an idea about the detection linearity of the proposed sensor. The linearity obtained is given in Fig. 4.16. From the corresponding equation and calculation of the slope, it is evident that the proposed sensor has a high degree of linearity. From the experimental data it is found that the detection linearity of the proposed sensor follows the following interpolation equation:

$$y(x) = 7770.3x - 10248. \tag{4.8}$$

It is also found that the detection linearity is 0.99911.

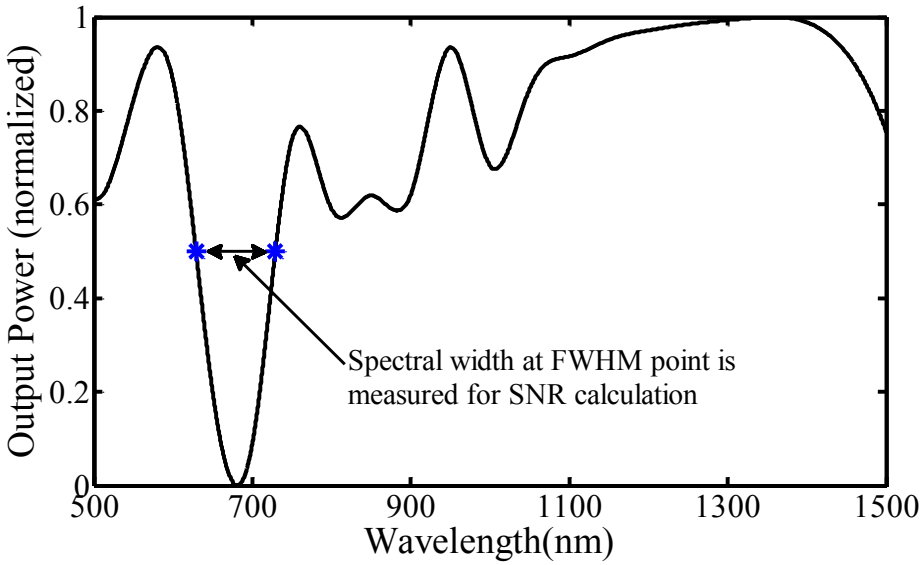

Fig. 4.15 The FWHM power point for SL-PCF based SPR sensor with single metal coating.

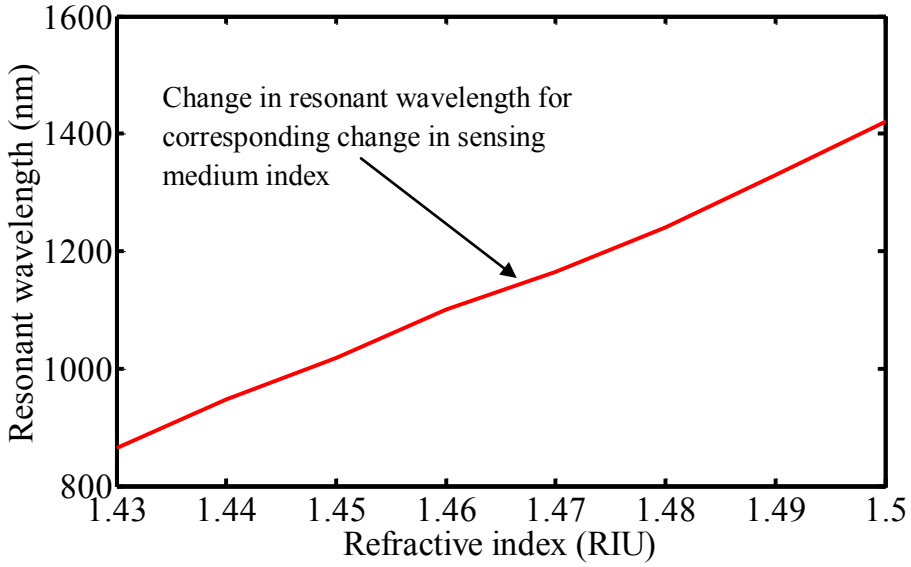

Fig. 4.16 Representation of detection linearity for proposed sensor design.

Being simpler in lattice structure, the proposed design is likely to provide less complexity in fabrication. The shift of resonance parameters with analyte effective index is highly linear. For very high detection linearity the proposed sensor can also be used as a calibration sensor with which the analyte refractive index can be retrieved from the calibration relations.

4.4 Effects of varying the width of gold coating

The effects of the width of the metal coating in the analyte channel is evaluated with 40, 50 and 60 nm of gold coating. The proposed design with varying width of analyte

channel coating is evaluated in terms of the variation in the sensitivity, shift of resonanc wavelength and shift in loss peak.

Keeping all other design parameter fixed, only the width of the gold coating is varied. This design is intended to see the effect of the width of the gold coating on coupling between core guided fundamental mode and plasmonic mode in analyte channel. The simulation procedure described in section 4.3 is followed here also. For each individual design, dispersion relationship between core guided fundamental mode and plasmonic mode is evaluated with varying width of the gold coating as given is fig. 4.17. It is evident from Fig. 4.17 that the resonance wavelength has shifted towards the longer wavelength range with the increase in the width of the analyte channel gold coating. Additionally the effect of gradual increase of the width of the analyte channel gold coating on the confinement loss is evaluated and is shown in Fig 4.18. As the evanescent field also decays exponentially away from the surface, to travel to large thickness of the gold coating the evanescent filed will become weaker resulting in weaker coupling between evanescent wave and plasmonic wave. So, for weaker coupling the core guided mode will suffer less loss. It is evident from Fig 4.18 that analyte channel with thicker gold coating resulted in lesser loss encountered by core guided fundamental mode.

Another consequence of the increase in the width of the gold coating is the change of the modal refractive index as shown in Fig. 4.17, leading to the shift of a loss peak towards longer wavelengths as given in Fig. 4.18. When the width of the gold coating increases, the value of the real part of the plasmonic mode effective indices increases. For increase in these values, now the cross section between the plasmonic mode and the core guided fundamental mode will occur in the longer wavelength range which also confirms the shift of the loss peak towards the longer wavelength range as shown in Fig. 4.18.

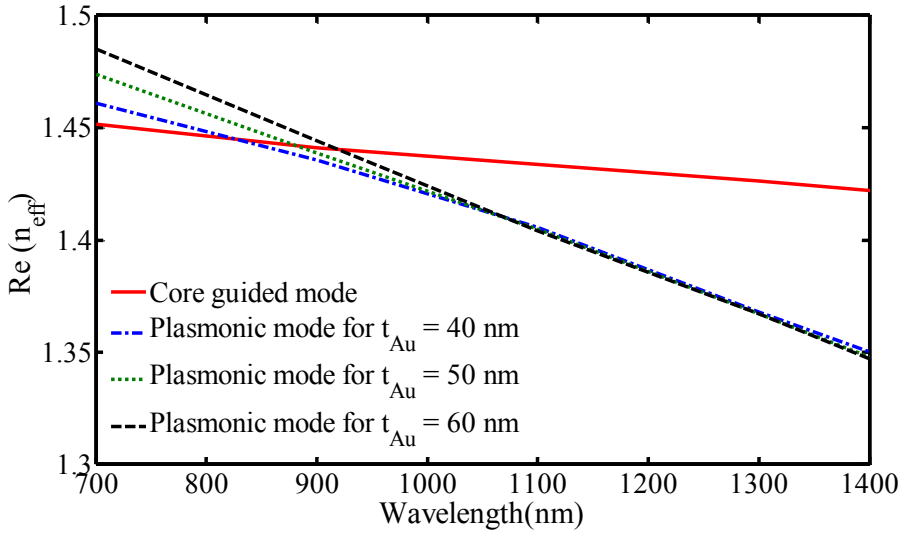

Fig. 4.17 Shift of resonance wavelength on varying width of gold coating.

The effect on the sensitivity with increasing width of the gold coating has also been evaluated. The effect is shown graphically in Fig. 4.19. It is found that with the increase in the width of the gold coating the corresponding sensitivity decreases. With the increase in the width of gold coating, the confinement loss decreases which indicate weaker coupling, leading to reduced sensitivity as confirmed in Fig. 4.19.

The change in sensitivity with the change in gold coating width follows the following interpolation equation:

$$y = 0.42975x^3 - 43.797x^2 + 1250.1x. \quad (4.9)$$

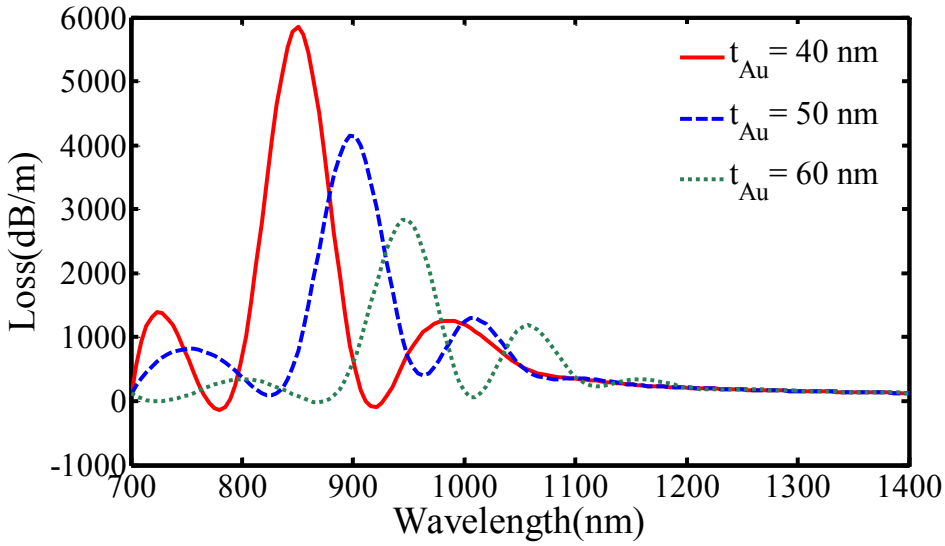

Fig. 4.18 Loss spectra of proposed PCF based SPR sensor in the vicinity of the first plasmonic peak for variation in gold layer thickness (t_{Au} = 40, 50 and 60 nm).

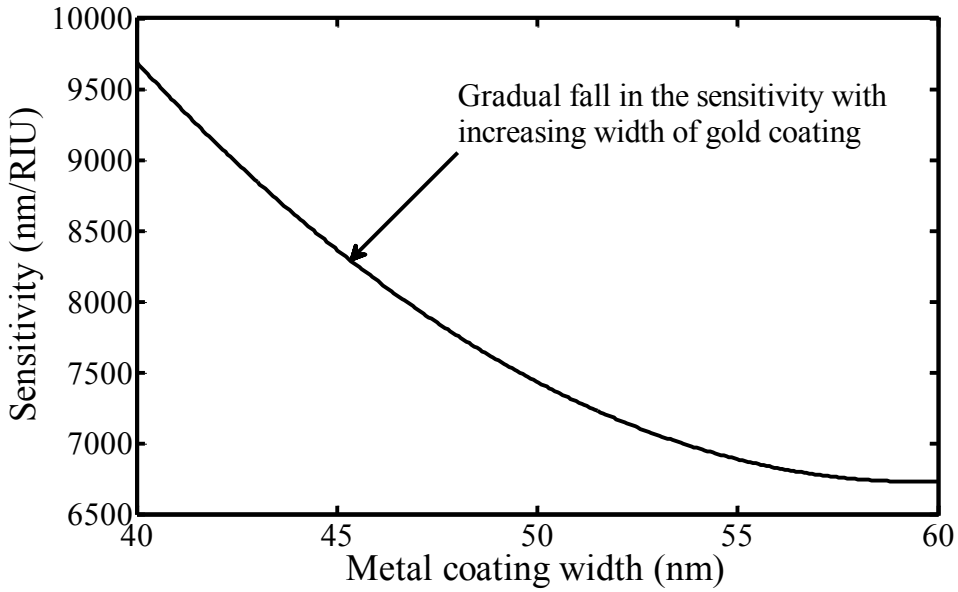

Fig. 4.19 Relationship between gold coating width and the sensitivity.

The analysis carried out with the varying width of the gold coating indicates the suitable range of operation wavelength for particular analyte index. As with the increase in the gold coating, the operating range shifts towards the higher wavelength range, the desired range of operation for any particular operation can be found out. In accordance with Fig. 4.17, there is a shift of the sensitivity peak (phase-matching wavelength) towards longer wavelengths. Again as depicted in Fig. 4.18, it is understood that with the increase in the width of gold coating, the confinement loss reduces. Furthermore, it is found that the sensitivity also depends on the width of the gold coating as shown in Fig. 4.19. Overall sensitivity decreases when the metallic layer becomes thicker. This fact is simple to understand. When the metallic layer thickness becomes significantly larger than that of a metal skin depth (~30-40 nm), the fiber core mode becomes significantly screened from plasmons, resulting in a low coupling efficiency, and, as a consequence, low sensitivity.

4.5 Effects of different metals in analyte channel coating

Besides gold, capability of other metals such as silver (Ag) and copper (Cu) for SPR sensor applications has also been analyzed. Both metals have the ability to be used for SPR sensor. Copper has some limitations like silver. It is chemically vulnerable against oxidation and corrosion, therefore, its protection is required for a stable sensing applications. Same design of the proposed SL-PCF based sensor is used for this investigation. Only instead of gold, silver is used in analyte channel coating to evaluate the effect of this metal coating on sensitivity. The complex refractive index of silver is also found using the Drude model. Like gold, 40 nm silver coating is used. As silver has a different complex refractive index profile than gold, it is expected that it will bring some interesting observation in terms of coupling and loss spectra of the output optical power profile.

The coupling between fundamental mode and plasmonic mode has been found out. The resonance wavelength is found out through wavelength interrogation method. Due to the change in the analyte refractive index, the shift of resonance wavelength is found out. This shift in resonance wavelength gave the sensitivity of this sensor with silver coating in analyte channel. The numerical results obtained through the simulation yields an average sensitivity of 6849 nm/RIU. The results obtained from the simulated model and from data interpretation suggests that the use of silver instead of gold reduces the sensitivity, as the use of silver reduces the amount of shift in the resonance wavelength. Instead of gold, if we use silver, it will reduce the spectral width of the resonance curve which ultimately increases the SNR or detection accuracy of the sensor.

In case of copper also, the same design is used. Only copper is used instead of silver for analyte channel coating. To evaluate the sensitivity using copper coating, we need the resonance wavelength at which the coupling between fundamental mode and plasmonic mode happens. The resonance wavelength is found out through wavelength

interrogation method. The shift of resonance wavelength for corresponding change in the analyte index is found out. The amount of shift in resonance wavelength gave the sensitivity of this sensor with copper coating. The numerical results obtained through the simulation yields an average sensitivity of 5762 nm/RIU.

If we investigate the dispersion curve for gold, silver and copper, we find that there is significant shift of the core guided fundamental mode effective index resulting a change in the sensor sensitivity. As an example, the shift in the refractive index at a particular resonance wavelength say 0.90 μm can be compared. In this resonance wavelength, gold has real part of effective refractive index with a value of 1.440976, while silver and copper has 1.441002 and 1.441035, respectively. We can find an increase in the value of the effective refractive index of silver followed by copper while comparing with gold. The exhibit of the shift in the core guided fundamental mode effective indices is given in Fig. 4.20. The power transmitted after coupling between core guided fundamental mode and plasmonic mode gives us the insight about the effect of the particular material on the sensitivity. The change in the power transmitted can also be compared for using different metal. The power output is normalized for easy assimilation. Power output is normalized with the power output of gold and found that the use of silver and copper has resulted a higher value of normalized power of 0.08706 and 0.3915, respectively. More transmitted power indicates weaker coupling between core guided mode and plasmonic mode resulting less sensitivity as confirmed later. Normalized transmitted power spectra for gold, silver and copper coating is given in Fig. 4.21. It denotes that the gold suffers the highest loss, followed by silver and copper which indicates that gold promises the best sensitivity amongst these three metals followed by silver and copper.

The results obtained from the simulated model and from data interpretation suggests that the use of silver and copper instead of gold reduces the sensitivity, as the use of silver and copper reduces the amount of shift in the resonance wavelength. But the use of silver and copper has shown some decrease in spectral width. Instead of gold, if we use silver or copper we can narrow down the resonance curve in the FWHM point which ultimately increases the detection accuracy or SNR of the sensor. But as both the metal has the disadvantage of less sensitivity than gold and as both of them are prone to oxidation and chemical instability, the independent use of silver or copper in analyte channel coating is likely to remain very limited. But the use of these metals with gold as bimetallic combination may give some added improvement in SNR, besides the advantage of gold of higher sensitivity. To investigate the SNR improvement by using silver, bimetallic combination of gold and silver has been investigated in the later section.

The effect of varying width of the metal coating on different metal namely gold, silver and copper has been evaluated. The evaluation shows that with the increase of the metal coating, the sensitivity decreases which conforms to the theory of SPR sensing. As the width of the metal layer increases, the coupling between the evanescent field

and the core guided fundamental mode decreases, so the sensitivity decreases. The result of the evaluation is plotted in the Fig. 4.22. The variation of sensitivity with the varying wifth of gold, silver and copper follows the folloing interpolation equations:

For gold: $$y = 0.42975x^3 - 43.797x^2 + 1250.1x, \quad (4.10)$$

For silver: $$y = 0.28715x^3 - 31.288x^2 + 963.3x, \quad (4.11)$$

For Copper: $$y = 0.28642x^3 - 30.237x^2 + 900.43x. \quad (4.12)$$

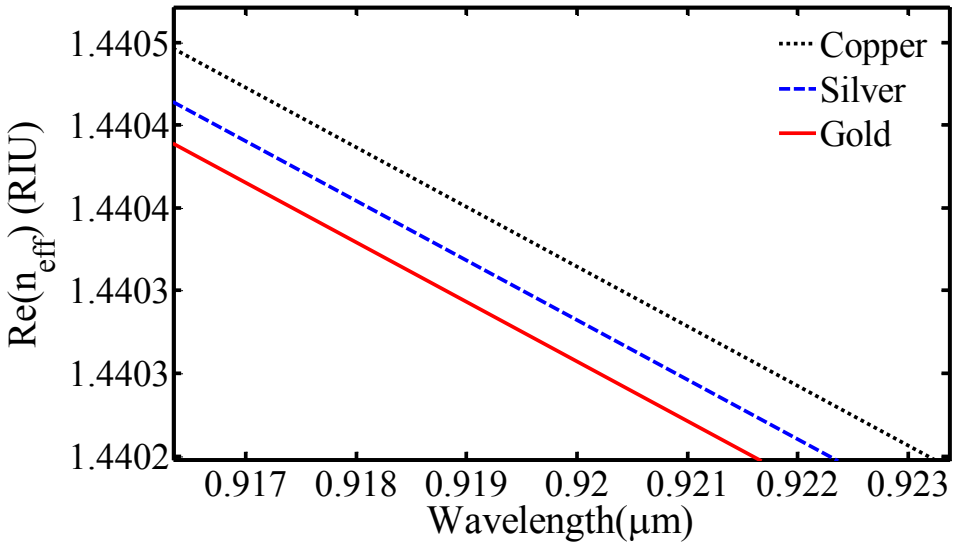

Fig. 4.20 Dispersion relation of the core guided fundamental mode while using gold, silver or copper for analyte channel coating.

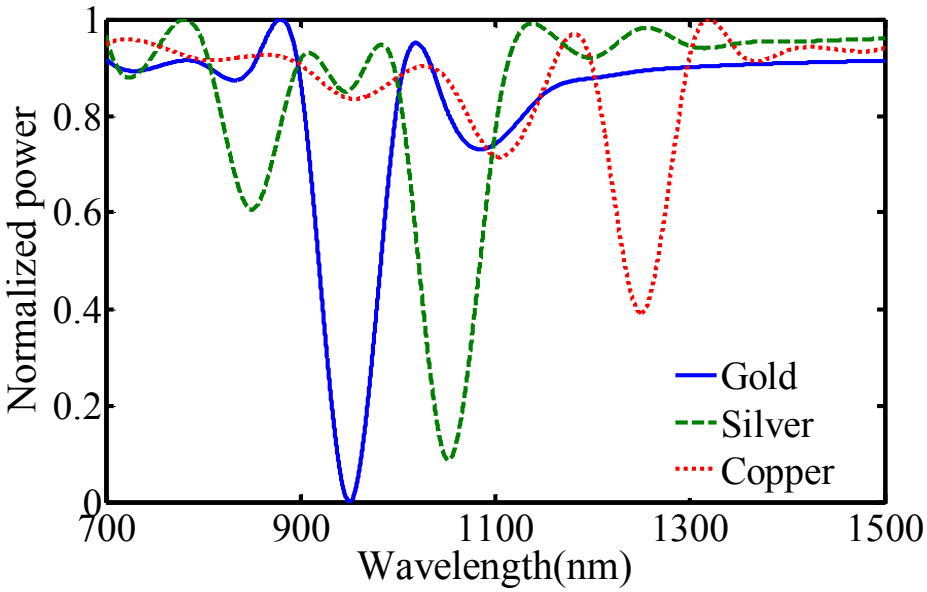

Fig. 4.21 The difference in output optical power while using gold, silver or copper for analyte channel coating.

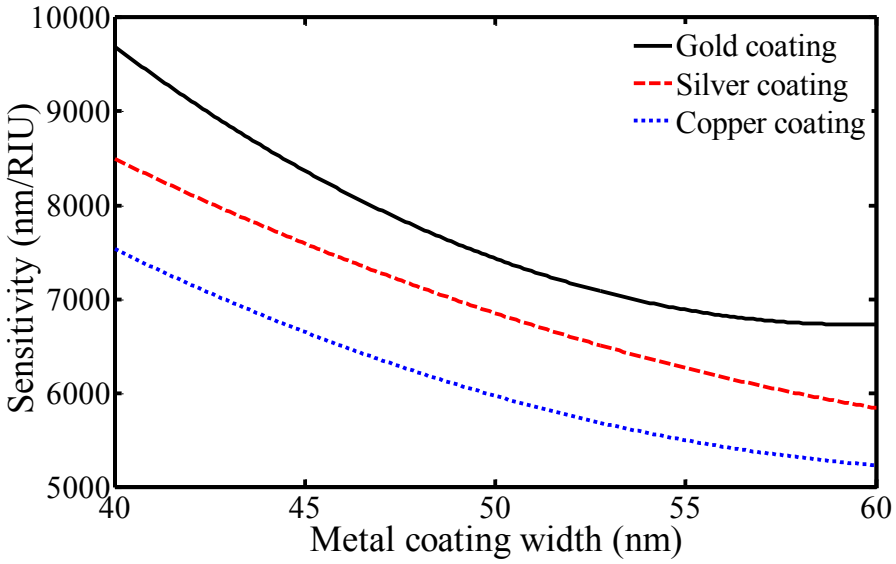

Fig. 4.22 Effects of metal coating width of different metals on sensitivity.

4.6 SPR sensor with bimetallic (Au-Ag) analyte channel coating

Gold demonstrated higher shift in the resonance parameters due to the change in refractive index of sensing layer and is chemically stable. Silver, on the other hand, displays a narrower resonance curve in terms of spectral width causing a higher detection accuracy or SNR of SPR sensor. Although silver promises better detection accuracy, it cannot be used alone for poor chemical stability. As gold promises better sensitivity and silver promises better detection accuracy, if we design a sensor with both gold and silver as bimetallic analyte channel coating, we may be able to achieve a sensor which has higher sensitivity and SNR. It is possible to find an optimum combination of gold and silver for achieving desired sensitivity and SNR. For evaluating the effect of different combination of the gold and silver, bimetallic layer consisting gold and silver was used. Schematic and the closer look of the analyte channel coating are given in Fig. 4.23 and 4.24, respectively.

In this investigation, we have used a bimetallic layer of 30 nm gold and 10 nm silver, where the gold coating is kept adjacent to the analyte channel. As we know that silver is not chemically stable, so silver is kept away from analyte channel and not allowing silver to be chemically active with any analyte which flows through the analyte channel. The concentration of power in the metal-analyte interface, produced due to the coupling between core guided fundamental mode and plasmonic mode is given in the Fig. 4.25. The presence of bimetallic layer is evident in the figure. The highest concentration of power is available in the metal-analyte boundary. From the dispersion relation we have brought out the resonance wavelength and subsequently the sensitivity was obtained. The SNR was evaluated from the FWHM power point in the normalised power profile. SNR was evaluated and compared with the single metal analyte channel. Bimetallic layer with a combination of 30 nm gold and 10 nm silver demonstrates an enhancement in sensitivity as well as SNR as shown in Fig. 4.26 and

4.27, respectively. For the effect of silver, the spectral width in the FWHM power point is reduced as expected.

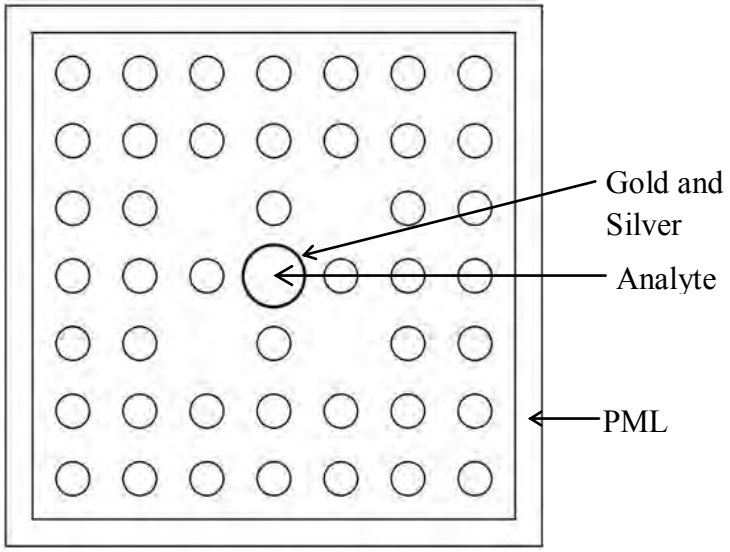

Fig. 4.23 Schematic cross section of the proposed SPR sensor with bimetallic layer of gold and silver.

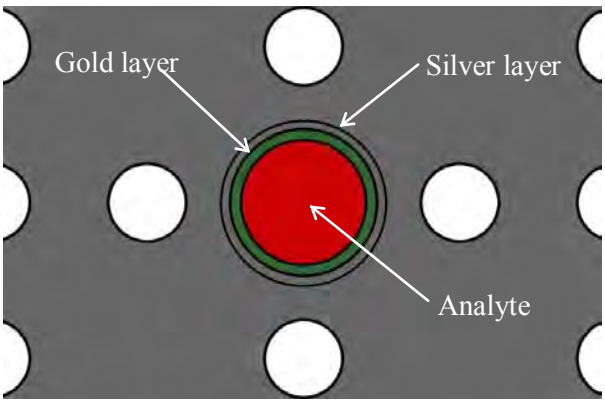

Fig. 4.24 Closer look of the bimetallic coating of gold and silver.

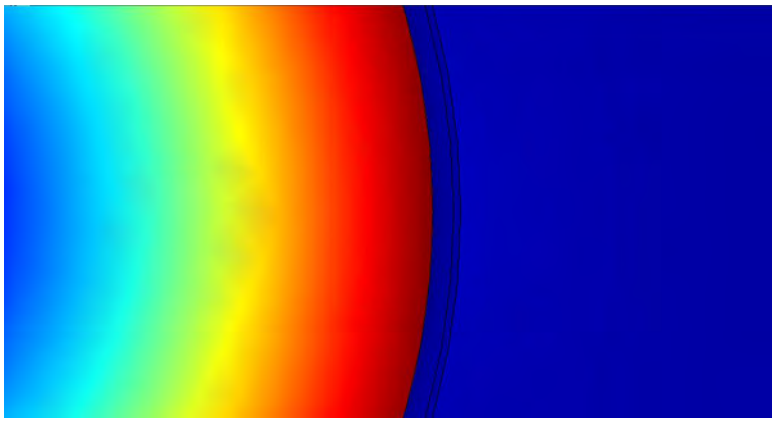

Fig. 4.25 Concentration of power in the metal-analyte boundary for plasmonic mode found in bimetallic (Au-Ag) analyte channel.

With pure silica material and single layer gold coating, sensitivity of 7432nm/RIU and SNR of 1.202 is achieved. Optimized design with bimetallic coating of gold and silver yields an average sensitivity of 13180 nm/RIU and SNR of 1.32. Exemplarily the enhancement of sensitivity in the analyte index range from 1.43 to 1.45 is given in Fig. 4.26. SNR improvement through narrowing of FWHM spectral width is shown in Fig. 4.27. So the use of bimetallic coating will enhance the sensitivity and SNR as well as reduce the gold consumption.

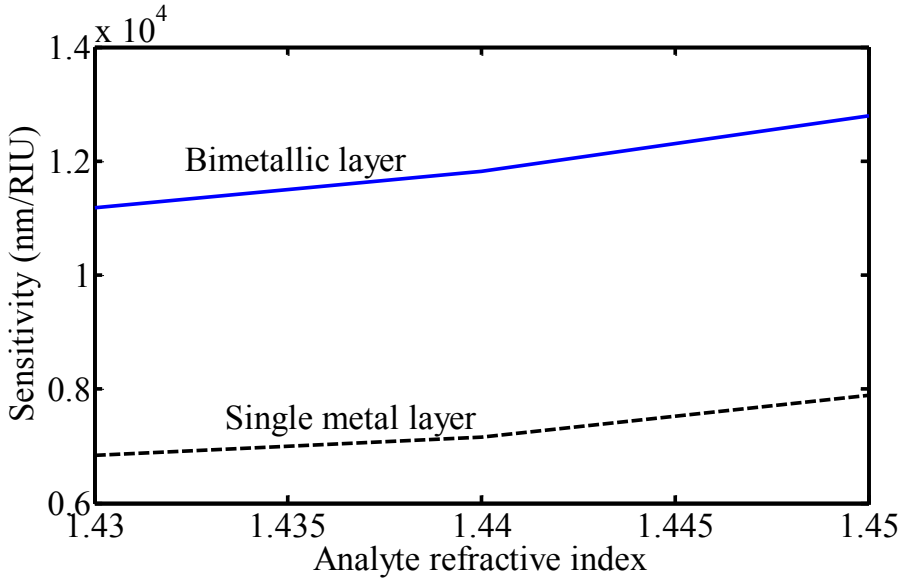

Fig. 4.26 Enhancement of sensitivity in bimetallic layer (30 nm gold and 10 nm silver) compared to single metal layer.

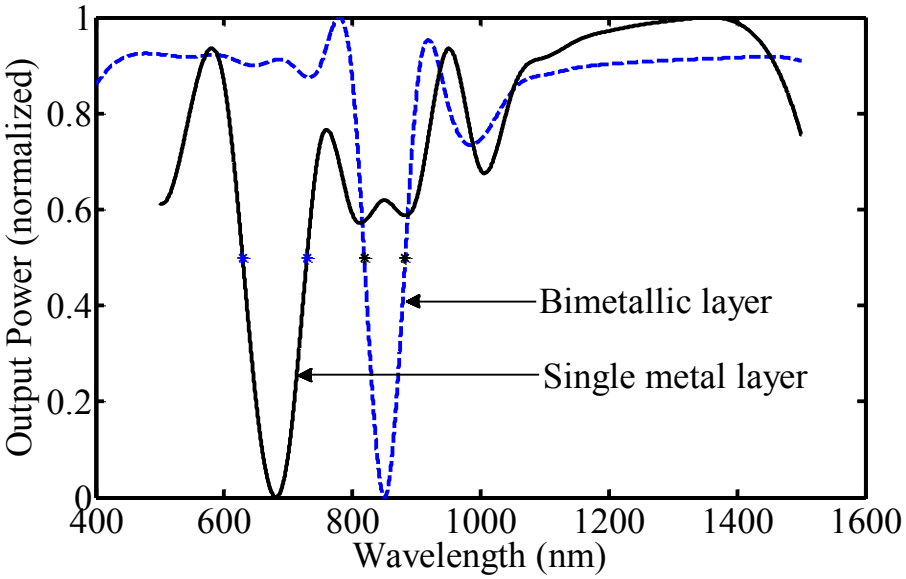

Fig. 4.27 Enhancement of SNR in bimetallic layer (30 nm gold and 10 nm silver) compared to single metal layer.

4.7 Effects of doping on the performance of PCF based SPR sensor

So far the proposed sensor has been evaluated using PCF made of pure silica. The analysis has been further extended by using different doping concentration with silica. 13.5% GeO_2, 9.1 % P_2O_5 and 5.2% B_2O_3 were used separately with pure silica. It was expected that the presence of dopants in the core of PCF will tune the sensitivity of the sensor. Dispersion in glasses with different dopants will give us the idea about the operating wavelength and also the possibility of tuning of the sensitivity. The dispersion curve is obtained from plotting the effective refractive index against the wavelength of operation for any particular analyte index. After plotting the dispersion we get the resonance wavelength and consequently the sensitivity. From the coupling between the core guided fundamental mode and plasmonic mode the resonance wavelength and the sensitivity was evaluated. Doping with 13.5% GeO_2, 9.1 % P_2O_5 and 5.2% B_2O_3 yielded a sensitivity of 8411 nm/RIU, 7026 nm/RIU and 6029 nm/RIU respectively as shown in Fig. 4.28. Interestingly it has been found that the effect of dopants on the sensitivity of the PCF based SPR sensor is same whether a single metal layer or a bimetallic layer is used. From the investigation it is found that the doping concentration has effect on the sensitivity of PCF based SPR sensor. 13.5 % GeO_2 has shown promise to enhance the sensitivity while other two dopants namely 9.1 % P_2O_5 and 5.2% B_2O_3 has not improved the sensitivity than the pure silica based SPR sensor.

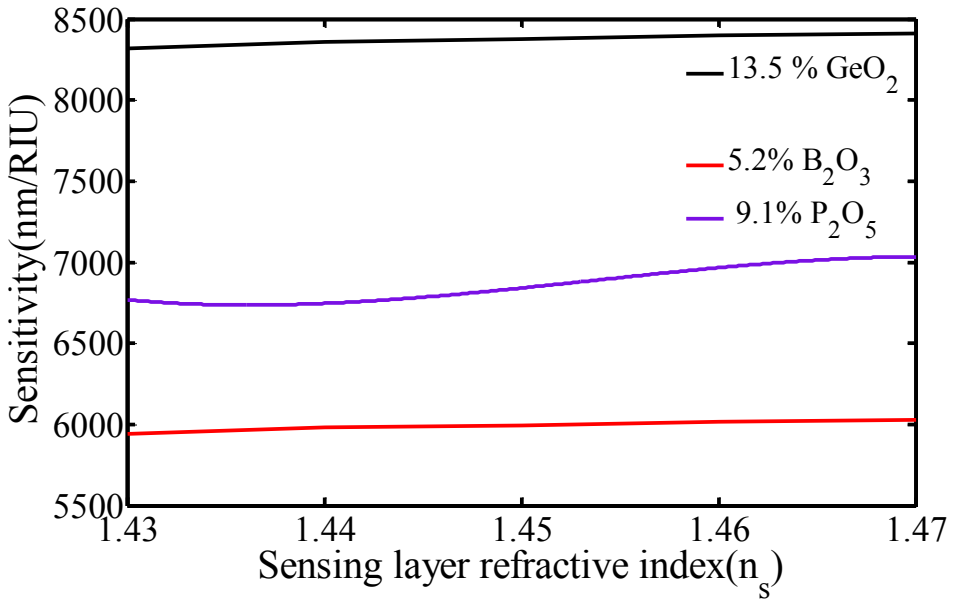

Fig. 4.28 Variation of sensitivity with variation of doping concentration.

4.8 Overall findings and comparison of results

The suitability of SL-PCF for SPR sensing system has been confirmed theoretically. With the use of SL-PCF, simplicity in design and fabrication procedure has been achieved. The use of SL-PCF based SPR sensor with only gold coating has yielded an

average sensitivity of 7432 nm/RIU. It has also been found that with increasing width of gold coating the sensitivity of the sensor decreases. It is found that besides gold, silver and copper can also be used for analyte channel coating. But silver and copper is needed to be covered with other metal to prevent oxidation and chemical reaction with analyte. So they can be used as a part of bimetallic coating. Amongst these three metals, gold demonstrated highest sensitivity, followed by silver and copper. But as silver and copper produced narrower resonance curve they are found to improve SNR while used with gold. Investigation with 13.5% GeO_2 doped silica has yielded an average sensitivity of 8411 nm/RIU. Additionally, extended investigation with bimetallic coating out of gold and silver has yielded an improved average sensitivity of 13180 nm/RIU. The results has been compared with other literature as given in Table 4.1. The results show encouraging improvement in the sensitivity in the sensing range of 1.43 to 1.50 refractive index. The dynamic detection capability over a wide range will enable this sensor to be suited for multiple applications and for multiple analyte detection. Application of this sensor will not be limited to detect a particular material rather it will be able to dynamically detect any material within a wide range of materials bearing refractive index from 1.43 to 1.50. This will also enable this sensor to be used in online monitoring of bimolecular detection without any labeling of the target molecules. In terms of SNR, with square lattice structure and single metal (gold) coating we have achieved a value of 1.202 which has been further enhanced by the use of bimetallic layer consisting of gold and silver. The use of silver in the bimetallic combination resulted in an optimized SNR of

Table 4.1 Comparison of various optical fiber and PCF based SPR sensor performance

Optical structure	Detection RI Range (RIU)	Wavelength of operation (nm)	Average Sensitivity (nm/RIU)	Ref.
Multimode fiber with S_iO film	1.4344-1.5859	700-1000	1023	[26]
Hexagonal lattice Solid core, MCHF	1.33-1.42	400-800	2929	[38]
	1.43-1.53	800-1850	9231	[38]
Liquid core, MCHF	1.50-1.53	700-1800	~5500	[39]
Analyte-filled core, HF	1.33-1.42	550-900	2775	[40]
Air hole in core. HF	1.33-1.41	500-850	2728	[41]
Polished multimode fiber	1.328-1.345	550-750	956	[49]
SMF, tilted grating	1.4211-1.4499	1525-1545	454	[50]
Square lattice, multi-core PCF, bimetallic layer coated channel	1.43-1.50	700-1800	13180	This work

1.32. The sensor also achieved a very high detection linearity (0.99911) which will allow it to be used as calibration sensor. By retrieving the resonance wavelength from the optical spectrum analyzer, corresponding refractive index of the analyte can also be retrieved from this calibration relations made out of calibration sensors.

CHAPTER 5

CONCLUSION

5.1 Conclusion of the work

This thesis made an endeavor to explore the suitability of SL-PCF to be used in SPR sensing probe. In particular, besides evaluating the suitability of SL-PCF, the primary aim was to enhance the sensitivity. Initially, different sensor probe based on H-PCF is being investigated. Later, multi-core SL-PCF based sensor with gold layer was evaluated. This design provided benefit in terms of structural simplicity and enhancement in sensitivity than that of H-PCF.

To enumerate the effects of varying width of gold coating on sensitivity, separate investigation is done. The obtained results show that with the increase in the width of gold coating, the sensitivity of the proposed sensor reduces which conforms the theory of coupling between core guided mode and plasmonic mode. Besides gold, silver and copper has been evaluated for its suitability in analyte channel coating. Silver and copper demonstrated weaker coupling between core guided mode and the plasmonic mode, resulting in lower sensitivity. But interestingly enough, they produce lesser spectral width in the output power which provided better detection accuracy than gold. Though silver and copper promised better detection accuracy, due to oxidation and chemical instability they cannot be used independently. But they may be used in combination with gold. Like varying width of gold, investigation with varying width of silver and copper is also being done. It has been found that the increase of the width of the silver and copper coating also reduces the sensitivity.

To obtain the advantage of higher sensitivity of gold and higher detection accuracy of silver a bimetallic layer composed of gold and silver was evaluated. Corresponding simulation and data interpretation with bimetallic analyte channel coating has provided better sensitivity and detection accuracy. Varying doping concentration consisting 13.5% GeO_2, 9.1% P_2O_5 and 5.2% B_2O_3 with pure silica were used individually and sensitivity was evaluated. The use of 13.5% GeO_2 promised enhancement in sensitivity while use of 9.1% P_2O_5 and 5.2% B_2O_3 didn't exhibit better sensitivity than pure silica.

It can be concluded that SL-PCF based SPR sensor is a promising candidate in SPR sensing regime. With the use of square lattice, simplicity in design and fabrication is achieved. Optimization of the design through bimetallic analyte channel coating with gold and silver promises better sensitivity and detection accuracy. The use of dopants especially 13.5% GeO_2 also promises better sensitivity. The obtained design has a sensitivity of 13180 nm/RIU in the sensing range of 1.43 to 1.50 RIU with high detection linearity. So a SL-PCF based SPR sensor with bimetallic analyte channel coating evolve as a candidate for future exploration, prototype fabrication and lab testing.

5.2 Scope for the future work

Though a number of design considerations have been evaluated, they could not be tested experimentally. Prototype development and experimentation can be done using the clean room facilities available in advanced lab thereby the numerical results may be verified experimentally which will strengthen the findings in this thesis. It is expected that any development that has been made to PCF based SPR sensor concepts and has been shown to work in simulations, would be demonstrated in working prototypes to verify the simulated results and would be an acclamation of the developed sensor concepts. Through experimentation, required design modification or optimization, if any, can be obtained and the resulted design can be recommended for future implementation.

SPR sensor with metal layers has been investigated here, which can be extended for metal nanoparticles separately or with allow combinations. As temperature can alter the behavior of silica, the effect of temperature on the PCF based SPR sensor performance can be evaluated. Basing on the change in behavior, this sensor can be evaluated for its utilization as temperature sensor.

SPR sensor can be implemented for a wide range of applications. Suitability of the proposed sensor for application specific utilization can be evaluated separately. As an example, using of this sensor in biolayer detection warrants the measurement of the deposition of the measurand in the metal-dielectric interface. So, after general evaluation for the suitability, application specific investigation can be carried out for optimizing the structure for particular use. Investigation of the suitability of the proposed sensor as biosensor and implementation of the required modification and optimization can be a major work ahead.

REFERENCES

[1] Hayashi, S. and Okamoto, T., "Plasmonics: visit the past to know the future," J. Phys. D: Appl. Phys., vol. 45, no. 433001, pp. 1-24, 2012.

[2] Sharma, A. K., Jah, R. and Gupta, B. D., "Fiber-optic sensors based on surface plasmon resonance: A comprehensive review," IEEE Sensors J., vol. 7, no. 8, pp. 1118-1129, Aug. 2007.

[3] Maier, S. A., Plasmonics: Fundamentals and Applications, New York: Springer, 2007, pp. 21-24.

[4] Homola, J., Surface Plasmon Resonance Based Sensors, Berlin: Springer, 2006, pp. 45-69.

[5] Adam, P. et al., "Surface Plasmons for Biodetection," in Photonic Sensing Principles and Applications for Safety and Security Monitoring, Xiao, G. and Bock, W. J., Eds. New Jersey: John Wiley & Sons, 2012, pp. 12-23.

[6] Pitarke, J. M., Silkin, V. M., Chulkov, E. V. and Echenique, P. M., "Theory of surface plasmons and surface-plasmon polaritons," Rep. Prog. Phy., vol. 70, pp. 1-87, 2007.

[7] Tudos, A. J. and Schasfoort R. B. M., "Introduction to Surface Plasmon Resonance," in Handbook of Surface Plasmon Resonance, Schasfoort, R.B.M. and Tudos, A. J., Eds. Berlin: Springer, 2008, pp. 1-14.

[8] Hassani, A. and Skorobogatiy, M., "Design of the microstructured optical fiber-based surface plasmon resonance sensors with enhanced microfluidics," Opt. Express, vol. 14, no. 24, pp. 11616–11621, Nov. 2006.

[9] Udd, E., "Overview of fiber optic sensors," in Fiber Optic Sensors, Francis T. S. Yu and Shizhuo Yin, Eds. New York: Marcel Dekker, 2002, pp. 1-3.

[10] https://www.biacore.com/lifesciences/products/systems_overview/Biacore_T200/System-Information/index.html.

[11] Kashyap, R. and Nemova, G., "Surface Plasmon Resonance-Based Fiber and Planar Waveguide Sensors," J. Sensors, vol. 09, no. 645162, pp. 1-9, 2009.

[12] Srivastava, S. K. and Gupta, B. D., "Fiber optic plasmonic sensors: past, present and future," The open Opt. J., vol. 7, pp. 58-83, 2013.

[13] Jha, R., Verma, R. and Gupta. B. D., "Surface plasmon resonance-based tapered fiber optic sensor: Sensitivity enhancement by introducing a teflon layer between core and metal layer," Plasmonics, vol. 3, pp. 151-156, 2008.

[14] Diez, A., Andrés, M. V., Cruz, J. L., "In-line fiber-optic sensors based on the excitation of surface plasma modes in metal-coated tapered fibers," Sens. Act. B, vol. 73, pp. 95-99, 2001.

[15] Slavík, R., Homola, J., Ctyroký, J. and Brynda, E., "Novel spectral fiber optic sensor based on surface plasmon resonance," Sens. Act. B, vol. 74, pp.106–111, 2001.

[16] Hoa, X. D., Kirk, A. G. and Tabrizian, M., "Towards integrated and sensitive surface plasmon resonance biosensors: A review of recent progress," Biosens. Bioelectron., vol. 24, no. 6, pp. 1667-1673, 2009.

[17] Iga, M., Seki, A. and Watanabe, K., "Gold thickness dependence of SPR-based hetero-core structured optical fiber sensor," Sens. Act. B, vol. 106, no.1, pp. 363–368, Apr. 2005.

[18] Wang, S. F., Chui, M. H. and Chang, R. S., "Numerical simulation of a D-type optical fiber sensor based on the Kretschmann's configuration and heterodyne interferometry," Sens. Act. B, vol. 114, pp. 120–126, 2006.

[19] Sharma, A. K. and Gerhard J. M., "Fiber optic sensor based on surface plasmon resonance with Ag-Au alloy nanoprticle films," Nanotechnology, vol. 17, no. 1, pp. 124-131, 2006.

[20] Tripathi, S. M, Kumar, A., Marin, E. and Meunier, J. P., "Side-polished optical fiber grating-based refractive index sensors utilizing the pure surface plasmon polaritons," J. Lightw. Technol., vol. 26, pp. 1980-1985, 2008.

[21] Ran, Z., Rao, Y., Zhang, J., Liu, Z. and Xu, B., "A miniature fiber-optic refractive index sensor based on laser-machined Fabry-Perot interferometer tip," J. Lightw. Technol., vol. 27, pp. 5426-5429, 2009.

[22] Dhawan, A., Gerhold, M. and Muth, J., "Plasmonic structures based on subwavelength apertures for chemical and biological sensing applications," IEEE Sensors J., vol. 8, no. 6, pp. 942-950, 2008.

[23] Allsop, T., Neal, R., Rehman, S., Webb, D. J., Mapps, D. and Bennion, I., "Generation of infrared surface plasmon resonances with high refractive index sensitivity utilizing tilted fiber Bragg gratings," Applied Optics, vol. 46, no. 22, pp. 5456-5460, 2007.

[24] Nemova, G. and Kashyap, R., "Theoretical model of a planar integrated refractive index sensor based on surface plasmon-polariton excitation with a long period grating," J. Opt. Soc. Am. B, vol. 24, no. 10, pp. 2696 – 2701, 2007.

[25] Verma, R. K., Sharma, A. K and Gupta, B. D., "Surface plasmon resonance based tapered fiber optic sensor with different taper profiles," Opt. Commun., vol. 281, no. 6, pp. 1486-1491, 2008.

[26] Zeng, J. and Liang, D., "Application of fiber optic surface plasmon resonance sensor for measuring liquid refractive index," J. Int. Mat. Sys. and Struct., vol. 17, no. 8-9, pp. 787-791, 2006.

[27] Kanso, M., Cuenot, S. and Louarn, G., "Sensitivity of Optical Fiber Sensor Based on Surface Plasmon Resonance: Modeling and Experiments," Plasmonics, vol. 3, pp. 49-57, 2008.

[28] Monro, T. M., Belardi, W., Furusawa, K., Baggett, J. C., Broderick, N. G. R. and Richardson, D. J., "Sensing with microstructured optical fibers," Meas. Sci. and Technol., vol. 12, pp. 854-854, 2001.

[29] Hoo, Y. L., Jin, W., Ho, H. L., Wang, D. N. and Windeler, R. S., "Evanescent-wave gas sensing using microstructure fiber," Opt. Eng., vol. 41, pp. 8-9, 2002.

[30] Cordeiro, C. M. B., Franco, M. A. R., Chesini, G., Barretto, E. C. S., Lwin, R., Cruz, C. H. B. and Large, M. C. J., "Microstructured-core optical fiber for evanescent sensing applications," Opt. Express, vol. 14, pp. 13056-13066, 2006.

[31] Webb, A. S., Poletti, F., Richardson, D. J. and Sahu, J. K., "Suspended-core holey fiber for evanescent-field sensing," Opt. Eng., vol. 46, no. 1, Jan. 2007.

[32] Jensen, J. B. et al., "Photonic crystal fiber based evanescent-wave sensor for detection of biomolecules in aqueous solutions," Opt. Lett. vol. 29, pp. 1974-1976, 2004.

[33] Smolka, S., Barth, M. and Benson, O., "Highly efficient fluorescence sensing with hollow core photonic crystal fibers," Opt. Express, vol. 15, pp. 12783-12791, 2007.

[34] Ritari, T., Tuominen, J., Ludvigsen, H., Petersen, J. C., Sorensen, T., Hansen, T. P. and Simonsen, H. R., "Gas sensing using air-guiding photonic bandgap fibers," Opt. Express, vol. 12, pp. 4080-4087, 2004.

[35] Skorobogatiy, M. and Kabashin, A., "Photonic crystal waveguide-based surface plasmon resonance biosensor," Appl. Phys. Lett., vol. 89, no. 143518, 2006.

[36] Hassani, A. and Skorobogatiy, M., "Design criteria for microstructured optical fiber based surface plasmon resonance sensors," J. Opt. Soc. Am. B, vol. 24, no. 6, pp. 1423–1429, June 2007.

[37] Gauvreau, B. et al., "Photonic bandgap fiber-based Surface Plasmon Resonance sensors," Opt. Express, vol. 15, no. 18, pp. 11413-11426, 2007.

[38] Shuai, B., Xia, L., Zhang, Y. and Liu, D. "A multi-core holey fiber based plasmonic sensor with large detection range and high linearity," Opt. Express, vol. 20, no. 6, pp. 5974-5986, Mar. 2012.

[39] Shuai, B., Xia, L. and Liu, D., "Coexistence of positive and negative refractive index sensitivity in the liquid-core photonic crystal fiber based plasmonic sensor," Opt. Express, vol. 20, no. 23, pp. 25858-25866, Nov. 2012.

[40] Zhang, Y. et al., "Microstructured fiber based plasmonic index sensor with optimized accuracy and calibration relation in large dynamic range," Opt. Commun. vol. 284, no. 18, pp. 4161–4166, Aug. 2011.

[41] Yu, X. et al., "A selectively coated photonic crystal fiber based surface plasmon resonance sensors," J. Opt., vol. 12, no. 1, 2010.

[42] Lee, H. W. H., "Plasmonic Photonic Crystal Fiber," Ph.D. Dissertation, Max Plank Inst. for the Sci. of light, Friedrich-Alexander University, Erlangen, Germany, 2012.

[43] Agrawal, G., Nonlinear fiber optics, fourth ed., California: Academic press, 2006, pp.15-49.

[44] Al-Bader, S. J., "Optical transmission on metallic wires−fundamental modes," IEEE J. Quantum Elctron., vol. 40, no. 3, Mar. 2004.

[45] Johnson, P. B. and Christy, R. W., "Optical constants of the noble metals," Phys. Rev. B, vol 6, no. 12, pp. 4370-4379, 1972.

[46] Sharma, A. K. and Mohr, G. J., "On the performance of surface plasmon resonance based fiber optic sensor with different bimetallic nanoparticle alloy combinations," J. Phys. D: Appl. Phys., vol. 41, 2008.

[47] Zynio, S. A., Samoylov, A., V., Surovtseva, E. R., Mirsky, V. M. and Shirsov, Y. M., "Bimetallic layers increase sensitivity of affinity sensors based on surface plasmon resonance," sensors, vol. 2, pp. 62-70, 2002.

[48] http://www.comsol.com/rf-module.

[49] Peng, W., Banerji, Y. C., Kim, Y. C. and Booksh, K. S., "Investigation of dual-channel fiber-optic surface plasmon resonance sensing for biological applications," Opt. Lett., vol. 30, no. 22, pp. 2988-2990, 2005.
[50] Shevchenko, Y. Y. and Albert, J., "Plasmon resonance in gold-coated tilted fiber bragg gratings," Opt. Lett., vol. 32, no. 3, pp. 211-213, 2007.